HIGH TEMPERATURE SUPERCONDUCTING
YBa$_2$Cu$_3$O$_{7-\delta}$
THIN FILMS AND BOLOMETERS

A Thesis Submitted to
the Graduate School of Engineering and Science of
İzmir Institute of Technology
in Partial Fulfillment of Requirements for the Degree of

MASTER OF SCIENCE

in Physics

by
Bülent ÖKTEM

May 2006
İZMİR

We approve the thesis of **Bülent ÖKTEM**

Date of Signature

---   **12 May 2006**
Prof. Dr. Doğan ABUKAY
Supervisor
Department of Physics
İzmir Institute of Technology

---   **12 May 2006**
Assoc. Prof. Dr. Mustafa TEPE
Department of Physics
Ege University

---   **12 May 2006**
Assist. Prof. Dr. Teoman YILDIZ
Department of Physics
Ege University

---   **12 May 2006**
Prof. Dr. Durmuş Ali DEMİR
Head of Department
İzmir Institute of Technology

Assoc. Prof. Semahat Özdemir
Head of the Graduate School

ACKNOWLEDGEMENTS

ABSTRACT

In this work, we report the results on the response characteristics of high temperature superconducting bolometers under the infrared and optical radiation. The bolometers were made of $YBa_2Cu_3O_{7-\delta}$ (YBCO) thin films deposited on <100>-oriented and $10x10x1-0.5$ mm^3 sized single crystal MgO substrates by using DC inverted cylindrical magnetron sputtering (ICMS) technique with 200 nm thickness. The thin films were characterized in detail by employing structural (XRD, SEM, EDX, and AFM), magnetic (χ-T) and electrical (R-T) measurements.

We have investigated effects of temperature and modulation frequency on the magnitude and phase of the infrared response of the both large and small area bolometers. Dependence of the phase and magnitude of the response of MgO substrate YBCO edge transition bolometers to a near infrared radiation on the superconducting transition width has also been investigated in this work. We have observed that the superconductivity transition width has major effects on the response of the bolometers such as; on a dip of the phase of the response versus modulation frequency curve around 1 Hz, the rate of decrease of the magnitude of the response, and dependence of the phase of the response on temperature at mid-range modulation frequencies.

Wavelength dependence of the photoresponse of YBCO edge transition bolometers has been studied. It was observed that the optical response of the devices was almost independent of the wavelength of incident light from 0.4 µm to 0.73 µm. Here we present the analysis and the possible mechanisms that can affect the response of the bolometers in the superconducting transition region.

ÖZET

Bu çalışmada yüksek sıcaklık süperiletken bolometrelerin kızıl ötesi ve görünür ışıma altında optik tepki karakteristikleri incelenmiştir. Bolometreler <100>-yönelimine sahip ve 10x10x1-0.5 mm^3 boyutlarında tek yönlü kristal MgO alttaşlar üzerine DC silindirik magnetron püskürtme tekniğiyle 200 nm kalınlığında büyütülmüş YBa$_2$Cu$_3$O$_{7-\delta}$ (YBCO) ince filmler üzerine yapılmıştır. İnce filmler XRD, SEM, EDX, ve AFM analiz yöntemleri kullanılarak yapısal, χ-T ölçümüyle manyetik, R-T ölçümüyle elektriksel olarak karakterize edilmiştir.

Sıcaklığın ve modülasyon frekansının küçük ve büyük alanlı bolometrelerin tepki fazı ve büyüklüğü üzerindeki etkileri araştırılmıştır. Bu çalışmada, MgO alttaşlar üzerine yapılmış YBCO kenar geçiş bolometrelerinin kızılötesi tepki fazlarının ve büyüklüklerinin süperiletken geçiş genişliğine bağımlılığı incelenmiştir. Süperiletken geçiş genişliğindeki değişimin bolometrelerin optik tepkisi üzerindeki gözlemlenen etkileri; 1 Hz civarında modülasyon frekansına karşı çizilen tepki fazı eğrisinde bir çukurun oluşması, tepki büyüklüğünün modülasyon frekansına göre azalma oranının artması ve orta modülasyon frekansı aralığında tepki fazının sıcaklığa bağımlı hale gelmesi olarak gözlemlenmiştir.

YBCO kenar geçiş bolometrelerinin dalgaboyuna bağımlılığı incelenmiştir. Aygıtın optik tepkisinin, üzerine gelen ışımanın dalga boyundan bağımsız olduğu 0.4 µm ile 0.73 µm dalgaboyu aralığında gözlenmiştir. Bu tezde, bolometrenin performansını etkileyen mekanizmalar ve bunların muhtemel sonuçları sunulmaktadır.

TABLE OF CONTENTS

LIST OF FIGURES

LIST OF TABLES

CHAPTER 1

INTRODUCTION

The discovery of superconductivity in 1911 opened a new era in the history of physics. Since then, this phenomenon has been intensively studied both theoretically and experimentally in order to reveal the true mechanism that gives rise to a disappearance of resistance and appearance of an ideal diamagnetic behavior of the material. Besides that huge amount of research efforts have been devoted to find ways to use them for practical applications. However, large-scale applications of superconductors have for long been limited by the necessity to cool the materials to boiling point of liquid helium, 4.2. It wasn't until the discovery of high-temperature superconductivity in 1986 that the research on superconductors took a major step forward. With the discovery of superconductivity in material classes showing transition to superconductivity at temperatures above liquid nitrogen temperatures the expectations from these materials in practical uses also came into major considerations. The high-T_c superconductors are interesting to study for several reasons. Developing a fuller understanding of superconductivity in the high-T_c regime is an important problem in solid-state physics. Secondly, the high-T_c superconductors have a large potential for applications both in large-scale and many areas of electronics, including quantum computers. Superconducting electronic devices have found many useful applications, especially with the developments in Josephson junction technology as in SQUIDs, Bolometers and tunnel junctions. Cooling by liquid nitrogen presented a major advantage over the low-T_c superconductors on their use in large scale applications, such as power cables. In view of electronic device applications the most widely studied high T_c material is $YBa_2Cu_3O_{7-\delta}$ (YBCO). Microelectronics components, in particular, require YBCO thin films. One of the successful methods to produce a high quality YBCO superconducting thin film is the DC magnetron sputtering technique. This technique is based on the ejection of atoms from the surface of a target material bombarding by energetic particles. The emitted atoms condense on a substrate forming a thin film.

High temperature superconductors due to their physical properties they became a good candidate for the fabrication of superconducting infrared detectors especially for bolometers. Using the magnitude of dR/dT in the superconducting transition of YBCO superconducting thin films makes possible to fabricate extremely sensitive bolometric

detectors for optical and infrared radiation. Bolometers are type of thermal detectors whose working principal is based on the change in their resistance as function of temperature. Applications of bolometers range from medical to agriculture and from military to space technologies.

In this study, dependence of the phase and the magnitude of the response of $YBa_2Cu_3O_{7-\delta}$ (YBCO) edge transition bolometers fabricated on single crystal MgO (100) substrates to a near infrared radiation on the superconducting transition width is presented. The bolometers were made of YBCO thin films of 200 nm thickness grown on single crystal MgO (100) substrates by inverted cylindrical magnetron sputtering. We have measured the responses of both large and small area devices with respect to the bias temperature and the radiation modulation frequency. We have observed that the superconducting transition width has major effects on the response of the bolometers such as; on a dip of the phase of the response versus modulation frequency curve around 1 Hz, the rate of decrease of the magnitude of the response, and the dependence of the phase of the response on temperature at mid-range modulation frequency. We have also investigated a correlation between the superconducting transition width and the YBCO film surface morphology of the devices. In this thesis, we present the analysis and the possible mechanisms that can affect the response of the bolometers at the superconducting transition region.

This thesis consists of four main parts. As the first part, in this chapter, some background information about the physical and optical properties of YBCO, substrates commonly used in the devices that will help the reader to understand the principles of the operation of the bolometers and the analysis for the observed phenomena during the measurements are given. The second chapter discusses working principle of high temperature edge transition bolometers. It defines the thermal parameters of bolometers. Traditional classic thermal model, simple RC model, and the latest advanced thermal model that uses the analogy between thermal and electrical parameters are introduced in this chapter. Chapter 3 is about the fabrication of bolometers, the characterization setup, and the measurement methods. The experimental results and analysis of the infrared response of the bolometers with respect to modulation frequency and temperature are discussed in the chapter 4.

1.1 Review of Superconductivity

One of the striking properties of superconductivity in materials is the vanishing electrical resistance below a certain critical temperature, T_c. This phenomenon was discovered in 1911 by Heike Kammerlingh Onnes while he was experimenting on liquid helium in order to study the behavior of metals at low temperatures. Much to everybody's surprise, the resistance of mercury dropped to an immeasurable low value when cooled below about 4.2 K. The material had passed into a new, superconducting state. The measurement results obtained by Onnes are shown in Figure 1.1 (Onnes 1911). Later, in 1913, he won the Nobel Prize for his research in this area.
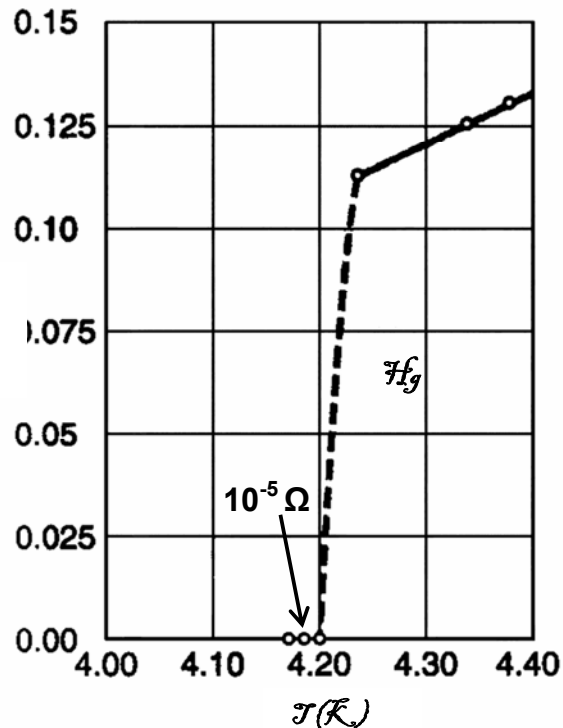
Figure 1.1: The electrical resistivity of mercury measured by Kammerlingh Onnes, showing for the first time the existence of zero resistance at 4.2 K, characteristic of superconductivity.

In 1933, Walter Meissner and Robert Ochsenfeld discovered another fundamental property of superconducting materials: when a superconducting material makes a transition from the normal to superconducting state, it completely excludes the magnetic field lines of an externally applied magnetic field from its interior. This phenomenon is known as diamagnetism and is today often referred to as the "Meissner

effect". The Meissner effect is so strong that a magnet can actually be levitated over a superconducting material.

The first widely accepted theoretical explanation of superconductivity was proposed in 1957 by American physicists John Bardeen, Leon Cooper, and John Schrieffer (Bardeen et al. 1957). They developed a microscopic theory, known as the BCS theory, explaining the physical mechanism of superconductivity. They were awarded with a Nobel Prize for this work in 1972. According to the BCS theory, superconductivity results from the interaction between electrons and the surrounding ionic crystal. When moving in the crystal, an electron leaves behind a deformation cloud which affects the positions of the ion cores. This distortion creates an effective positive charge which attracts other approaching electrons to form an electron pair, called Cooper pair. The Cooper pairs move without scattering in the lattice, which leads to the resistance-free nature of the superconducting state. However, the BCS theory has become inadequate to explain how superconductivity is occurring in high T_c superconductors.

Another significant theoretical advancement came in 1962 when Brian D. Josephson, a graduate student at Cambridge University, predicted that electrical current would flow between two superconducting materials even when they are separated by a non-superconductor or insulator (Josephson 1962). His prediction was later confirmed and won him a share of the 1973 Nobel Prize. This tunneling phenomenon is today known as the "Josephson Effect" and has been applied to electronic devices such as the SQUID, an instrument capable of detecting even the weakest generated magnetic fields such as those from the human brain.

Many elements, alloys, and compounds are known to be superconducting when cooled below a specific critical temperature. Most of the materials have a very low T_c and thus cooling to the temperature of liquid helium (4.2 K) is usually required. For long, such a low temperature restricted the number of potential commercial applications of superconductors. For this reason, there was an enormous interest in discovering new superconducting materials that would have a higher transition temperature. In 1986, a new era was opened in the field of superconductivity by the synthesis of a brittle ceramic compound Lanthanum Barium Copper Oxide (LBCO) with a critical temperature of 36 K. Up to this breakthrough, the highest recorded transition temperature in superconductors was 23.3 K for thin film of Nb_3Ge and the new material found was pretty interesting because BCS theory had predicted a theoretical limit of about 30-40 K for T_c due to the thermal vibrations. The discovery was so remarkable

that not only because it represented a significant increase in the critical temperature but also because the material $La_{2-x}Ba_xCuO_4$ was the first cuprate member of a new class of materials known as copper oxide superconductors (Bednorz and Muller 1986) exhibiting superconductivity. The discovery of these superconducting copper-oxides (cuprates) won, J. Georg Bednorz and K. Alexander Müller, the Nobel Prize in the following year. Since ceramics are normally antiferromagnetic insulators, no scientist had considered them as potential high-temperature superconductor candidates. Researchers around the world began "cooking up" ceramics for crystallization of every imaginable combination in a quest for higher and higher critical temperatures, T_c. In 1987, a research team at the University of Alabama substituted Yttrium for Lanthanum in the Muller and Bednorz molecule and found another cuprate Yttrium barium copper oxide compound $YBa_2Cu_3O_{7-x}$ (YBCO) with an incredible $T_c = 92$ K, whose critical temperature is well above the boiling point of liquid nitrogen (Wu et al. 1987). Therefore, it enabled to use liquid nitrogen as a coolant instead of liquid helium. Soon after YBCO was discovered, the two bismuth strontium calcium oxide compounds (BSCCO) were found; $Bi_2Sr_2CaCu_2O_{8+x}$ (Bi-2212) and $Bi_2Sr_2Ca_2Cu_3O_{10+x}$ (Bi-2223) (Chu et al. 1988) with critical temperatures 85 K and 110 K respectively. The critical temperature reached to 127 K with discovery of Thallium Barium Calcium Copper oxide compound (TBCCO), $Tl_2Ba_2Ca_2Cu_3O_x$ (Tl-2223) (Hazen et al. 1988). At the present time, the world record T_c of 138 K is now held by a thallium-doped, mercuric-cuprate comprised of the elements mercury, thallium, barium, calcium, copper, and oxygen, $(Hg_{0.8}Tl_{0.2})$ $Ba_2Ca_2Cu_3O_{8.33}$ at ambient pressure (Dai et al. 1995). Under extreme pressure its T_c can be coaxed up even higher - approximately 25 to 30 degrees more at 300,000 atmospheres.

1.2 Physical Properties of $YBa_2Cu_3O_{7-\delta}$

Unlike the conventional elemental superconductors, the HTS materials have relatively complex crystal structures with a layered form and high degree of anisotropy. $YBa_2Cu_3O_{7-\delta}$ (YBCO) is one of the most thoroughly studied HTS materials and it is widely utilized in various fields of research. YBCO has numerous advantages compared to other ceramic superconductors such as;

- the only known stable four-element compound with a T_c above 77 K
- includes neither toxic elements (e.g., Hg) nor volatile compounds
- relatively easy to make single-phase YBCO in contrast to other HTS materials

- less anisotropic than other HTS materials, carries higher current densities at higher magnetic fields.

However, one clear disadvantage of the compound is that it degrades in humid environment, even in the ambient air.

1.2.1 Critical Parameters

The critical temperature is one of the most important parameters characterizing superconductors. Critical Temperature is defined as the temperature at which the superconductor loses its electrical resistance resulting in a virtually lossless flow of current. The range of the critical temperatures extends from 0.001 K for the element Rh to 138 K for the Hg-Th-Ba-Ca-Cu-O compound. Critical temperature is also a good way to divide superconductors into different classes. Low-temperature superconducting (LTS) materials have T_c below 30 K while the novel high-temperature superconducting (HTS) materials have T_c; ranging from 35 K to 138 K. Actually, the temperature of liquid nitrogen (77 K) is a more practical lower limit for HTS materials. Although the BCS theory explains well the origin of superconductivity in LTS materials, there exists no generally accepted microscopic theory for HTS materials (Anderson 1997). In particular, the microscopic pairing mechanisms in high-temperature superconductors are not fully known.

The superconducting state can be destroyed by applying a strong enough magnetic field H on the material. The threshold or critical value of the applied magnetic field for the destruction of superconductivity state is denoted by $H_c(T)$ and is a function of the temperature. By virtue of the critical magnetic field, we can categorize the superconductors in two types. In the case of type I superconductors, an external magnetic field higher than a certain critical field (H_c), destroys the superconducting state. The critical magnetic field is a function of temperature such that it tends to zero when the temperature is close to T_c. The relationship between T_c and H_c in specific for low T_c materials can be formulated as follows (Kresin and Wolf 1990).

$$H_C = \begin{cases} H_{c0}\left[1-\left(\dfrac{T}{Tc}\right)^2\right] & T \langle T_c \\ \\ 0 & T \geq T_c \end{cases}$$

(1.1)

where H_{co} is the value of the critical field at zero temperature.

6

Type II superconductors, on the other hand, have two critical fields: the lower and the upper critical fields; H_{c1} and H_{c2} respectively. If the applied field $H < H_{c1}$, the material is in the superconducting Meissner state. When the external magnetic field is between the two critical values, $H_{c1} < H < H_{c2}$, the material is in a mixed state and above H_{c2} the superconductivity of type II materials disappears completely as shown in Figure 1.2 (Akram 2000). In the mixed state, an external magnetic flux penetrates partly into the superconducting material in the form of vortices. The core of a vortex is in the normal state, whereas the other part of the material is still in the superconducting state. Each vortex carries a discrete amount of magnetic flux, namely one flux quantum, $\Phi_0 = 2.07 \times 10^{-15}$ Tm^2. A vortex has a normal core whose radius is the coherence length ξ and the magnetic field of the vortex decays on the characteristics distance of London penetration depth, λ. Superconductors can be classified into type I and type II materials by defining the Ginzburg-Landau parameter $\kappa = \lambda / \xi$. For all type I superconductors, κ should be smaller than $\sqrt{2}$, and for type II materials, κ should be greater than $\sqrt{2}$.
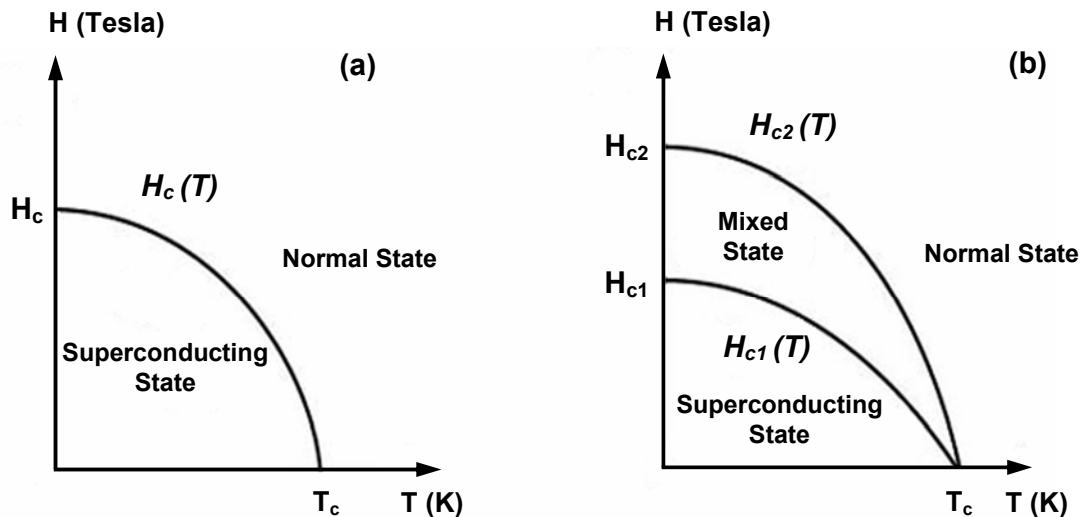
Figure 1.2: Critical magnetic field as a function of temperature for (a) type I and (b) type II superconductors.

HTS materials belong to type II superconductors, as well as some LTS alloys and compounds. The most important property of type II materials is that they have higher critical fields than type I materials, which makes them suitable for many advanced applications. In addition, their T_c is usually higher, even in the case of LTS materials.

Critical current density (J_c) is another key parameter of high-temperature superconductors, in particular for thin-film applications. There is a certain maximum current that superconducting materials can be made to carry, above which the superconducting state will be destroyed. If too much current is pushed through a superconductor, it will revert to the normal state even though it may be below its transition temperature. The value of critical current density, J_c, is a function of temperature; i.e., the colder you keep the superconductor the more current it can carry. The magnitude of the critical current density for YBCO thin films is typically $J_c \geq 1$ MA/cm^2 at 77 K, although values of almost 10 MA/cm^2 have been reported (Huhtinen et al. 1999). It depends on the nature and geometry of the system, and is related whether the magnetic field produced by the current exceeds the H_c of the system. In type II superconductors, if $J > J_c$, the vortices start to move in the material causing resistance and thereby losses. Fortunately, there are inhomogeneities in the material which can trap vortices and thus increase the value of J_c.

The Critical temperature, critical magnetic field, and critical current density are all inter-related. The phase diagram in Figure 1.3 demonstrates relationship between T_c, H_c, and J_c. The highest values for H_c and J_c occur at 0 K, while the highest value for T_c occurs when H and J are zero. When considering all three parameters, the plot represents a critical surface. From this surface, and moving toward the origin, the material is superconducting. Regions outside this surface the material is normal or in a mixed state. Notice that because of the mixed state, the phase diagram represents a Type II superconductor.

As the rest of high-T_c superconductors, YBCO is a type II superconductor. The flux of carriers along their CuO$_2$ layers causes anisotropy in these materials, whose properties are different in the *ab*-plane directions and the *c*-axis direction. Typical superconducting parameters of the YBCO thin films are shown in Table 1.1 where the subscripts refer to the different lattice directions.
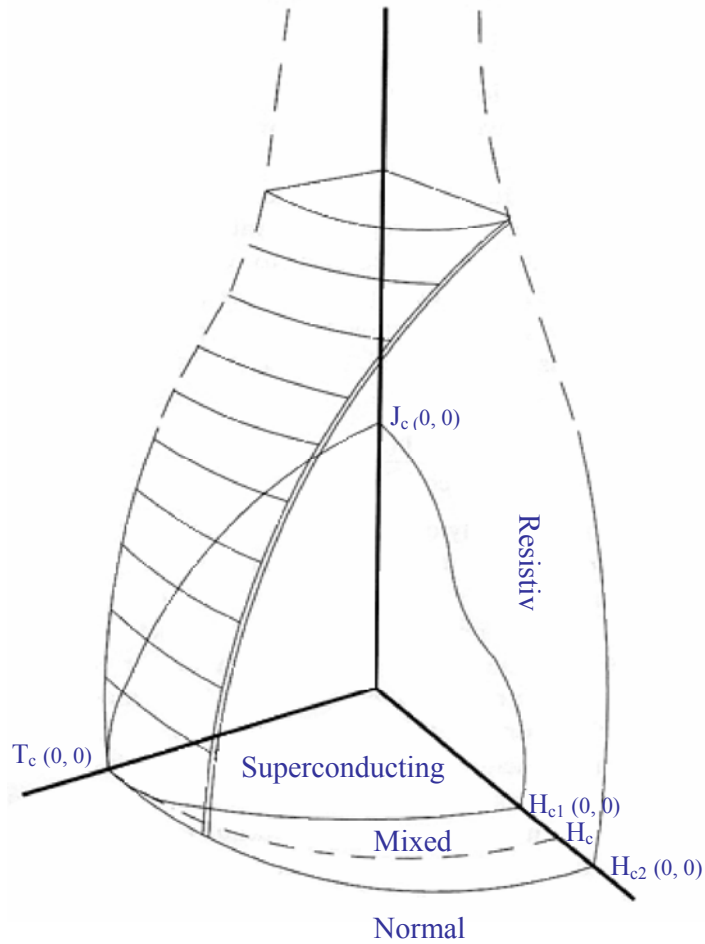
Figure 1.3: The critical surface for superconductivity of Type I and II superconductors

Table 1.1: Typical superconducting parameters of YBCO

Critical Temperature	90 - 92 K
Critical Magnetic Fields	$H_{c1}\ (0) = 10$ mT $H_{c2}\ (0) = 300$ T
Critical Current Density	≥ 1 MA/cm^2
Coherence lengths	$\xi_{a,b}(0) = 35$ Å $\xi_c\ (0) = 4$ Å
London Penetration Depths	$\lambda_{a,b}(0) = 30$ nm $\lambda_c(0) = 200$ nm

1.2.2 Lattice structure
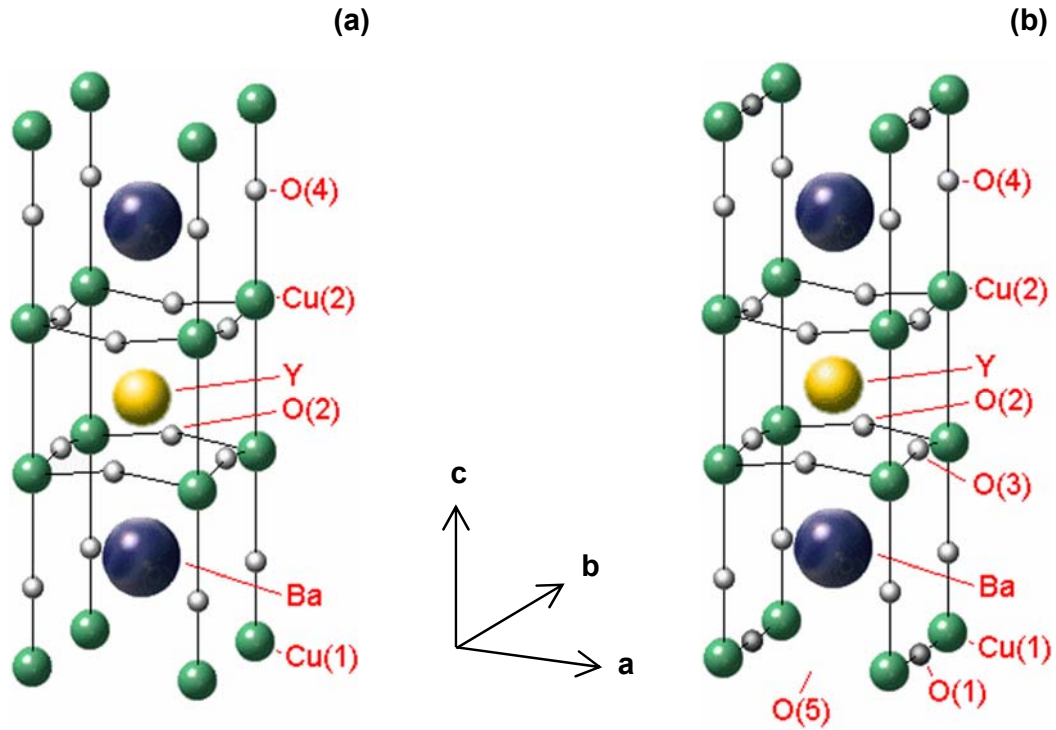
Figure 1.4: Schematic of the unit cell of $YBa_2Cu_3O_{7-\delta}$ (YBCO) crystal structure in (a) Tetragonal and (b) Orthorhombic phases.

$YBa_2Cu_3O_{7-\delta}$ can have two different lattice geometries. One is tetragonal structure which shows insulator properties and the other is orthorhombic structure that shows superconductor properties as shown in Figure 1.4 (Bozbey 2003). The change in oxygen content from $YBa_2Cu_3O_6$ to $YBa_2Cu_3O_7$ results in a phase transition in the material from a tetragonal antiferromagnetic insulator to an orthorhombic metal exhibiting superconductivity when the oxygen stoichiometry reaches about 6.4. When optimally doped, $\delta=0$, the CuO-chains are perfectly ordered and YBCO has an orthorhombic crystal structure, centered around two Cu-O planes. The planes are separated by a sparsely populated layer containing the Y atom. Superconductivity and charge transport in YBCO, as in all the high-Tc cuprates, is mostly confined to the Cu-O planes. The Cu-O planes lie in the ab plane of the crystal, and consist of Cu atoms strongly covalently bonded with four oxygen atoms, in a square-planar configuration.

On either side of these planes lies a region containing a Ba atom and Cu-O chains, separating the paired Cu-O planes by ~8.2 Å thick (Mischke 2003). The Cu-O chain layers also consist of Cu atoms bonded to four oxygen atoms in a square-planar configuration, but in the chain layers this configuration extends only in the b direction in the crystal.   The Cu-O planes and the Cu-O chains contribute to the superconductivity; CO_2 planes contain mobile charge carriers (holes) and the Cu-O chains acts as charge reservoir that transfer holes to the planes.

The oxygen atom missing when $\delta = 1$ disappears from the Cu-O chain layer. Superconductivity is lost even though the conduction layers, Cu-O planes, are unchanged. As oxygen is added, the chains grow. Long enough chains appear to be able to donate holes to the conduction planes, enabling superconductivity when the concentration is high enough. The orthorhombic phases might differ from each other depending on the oxygen content of the unit cell. For example, for $\delta = 0.01$, the single phase orthorhombic structure has lattice parameters $a = 3.821$ Å, $b = 3.887$ Å, and $c = 11.648$ Å (Bozbey 2003).

The term 7-δ in the chemical formula, $YBa_2Cu_3O_{7-\delta}$, appears because the CuO plane between the adjacent BaO layers is imperfect in the sense that there is a slight deficiency of oxygen. One reason for that kind of behavior is the mobility of the oxygen atoms. Mobility increases with increasing temperature, which means that δ is also a function of temperature.

When the temperature is higher, $\delta=1$ and YBCO has a tetragonal structure. Only the orthorhombic structure is superconducting but, unfortunately, it is stable only at temperatures below 500 ^{o}C. This complicates the deposition of thin films. Since the deposition has to be performed at high temperatures, a post-annealing is required so that the high-temperature tetragonal structure undergoes a phase transition to the orthorhombic structure. The transition temperature slightly depends on how much oxygen is present during the post-annealing step: at 1 mbar, the temperature is 800 ^{o}C and at 700 mbar, it is approximately 600 ^{o}C (Tuohiniemi 1999).

1.2.3 Resistance
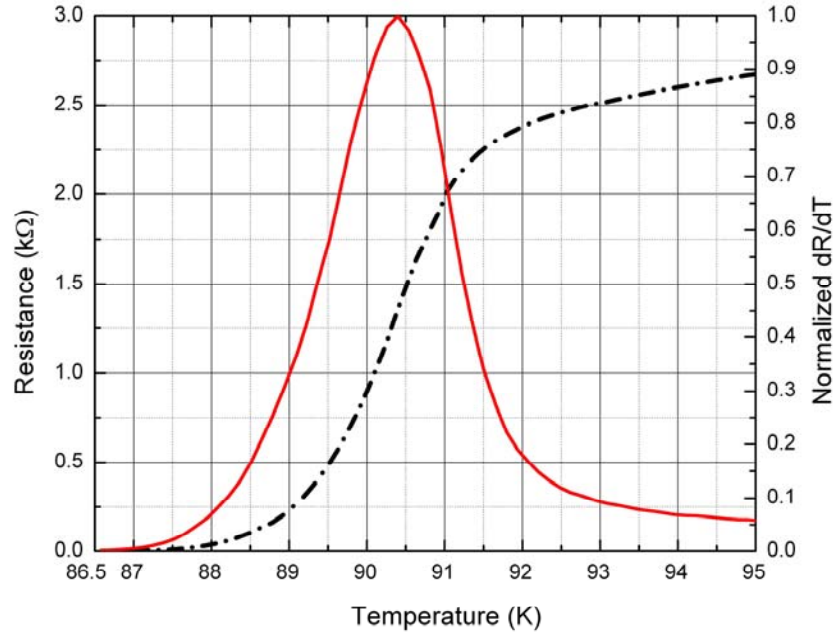
Figure 1.5: The resistance and normalized dR/dT graph of YBCO bolometer as a function temperature.

In the superconducting state, DC electrical resistivity is zero or close to zero at $T_{c\text{-}zero}$ that persistent electrical currents have been observed to flow without attenuation in the superconducting rings. Above the onset temperature of the superconducting transition, $T_{c\text{-}onset}$, resistance behavior of the YBCO materials are like metals and they have a rather linear resistance behavior as illustrated in Figure 1.5. The zero resistance temperature, $T_{c\text{-}zero}$, and onset temperature, $T_{c\text{-}onset}$, of YBCO thin films are determined from the 10% of the slope of the resistance versus temperature, dR/dT curve while the critical temperature, T_c, of the thin film can be obtained from the peak point of the dR/dT curve. Since the basic operating principle of a bolometer is related to the slope of the resistance versus temperature, the optimal operating temperature of a bolometer is the point where dR/dT is maximum. However, for our studies we biased the bolometers at various temperatures even at room temperature to see the temperature effect on the response of the devices.

1.2.4 Thermal Conductivity

In general, the low-temperature thermal conductivity of solids consists of two independent terms, the conductivity associated with the transport of charge carriers, K_{el}, and the conductivity arising from lattice vibrations, phonon, K_{ph}. The total thermal conductivity is then

$$K = K_{el} + K_{ph} \qquad (1.2)$$

In conventional metals electrons carry most of heat, so the phonon contribution to the thermal conductivity can be in many cases neglected. However, in high-T_c cuprates, K_{ph} can be the same order of magnitude as K_{el}, or even 10 times larger.
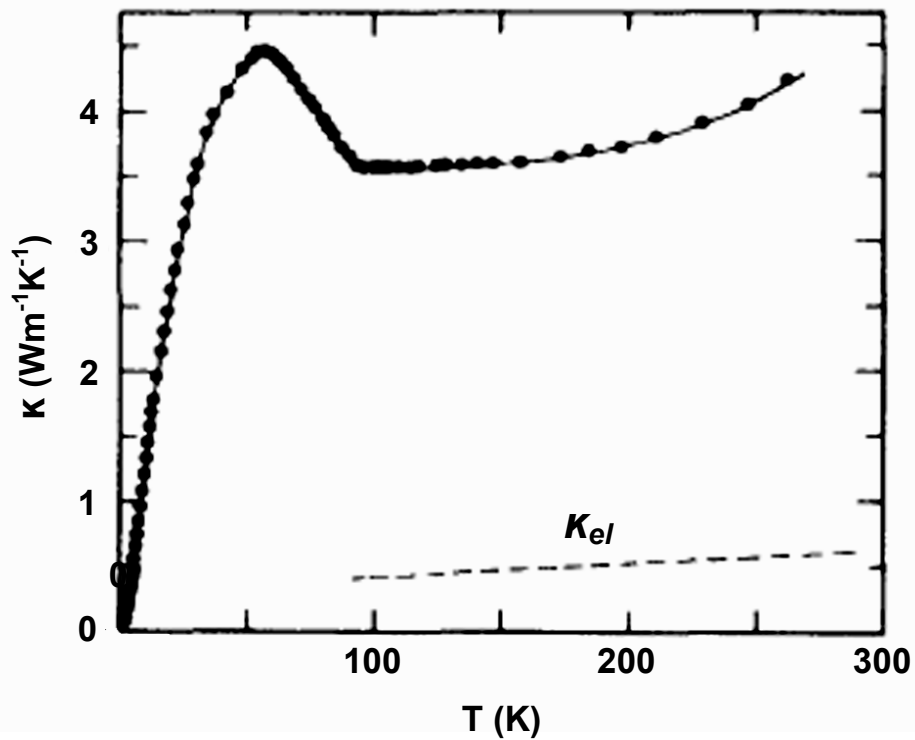
Figure 1.6: Thermal conductivity of YBa$_2$Cu$_3$O$_7$ (solid line) and the upper limit of electronic thermal conductivity (dashed line) K_{el} estimated from the electrical resistivity ρ.

It can be estimated that the electronic component of thermal conductivity K_{el} is obtained from the electrical resistivity ρ. Assuming an elastic scattering, an upper limit to the carriers' thermal conductivity, K_{el}, in the normal state can be calculated using the Wiedemann-Franz law, states that the ratio of the thermal conductivity to the electrical conductivity of a metal is proportional to the temperature,

$$K_{el} = L_0 T \rho^{-1} \tag{1.3}$$

where L_0 is the proportionality constant known as Lorenz number and is equal to 2.45×10^{-8} W·Ω·K^{-2} (Suleiman et al. 1993). The values of K_{el} with respect to temperature do not exceed 10% of the thermal conductivity as illustrated in Figure 1.6. Thus, the largest contribution to the total thermal conductivity around T_c seems to be due to the lattice conduction.

As shown in Figure 1.6, the electronic component of the thermal conductivity normally decays around transition temperatures as superconducting pairs form so they do not transport energy. On the other hand, there is the sudden increase of thermal conductivity in YBCO associated with the onset of superconductivity (Uher and Kaiser 1987). This can be explained by the increase in lattice thermal conductivity, K_{ph}, due to a reduction of scattering of phonons by carriers as they condense into cooper pairs. After the number of phonons starts to decrease with the further decrease of temperature, the thermal conductivity, K, starts to drop. Uher et al. (1987) found the values of thermal conductivity for YBCO 3.9 Wm-1K-1 and 3.5 Wm-1K-1 at 80 K and 90 K respectively.

1.2.5 Thermal Capacity

The heat capacity of a metal is made up of contributions due to the electrons and to the crystal lattice. At low temperatures, it is mostly the electrons that contribute. With decreasing temperatures, the electronic heat capacity decreases linearly, $C_{el} \sim T$, whereas the lattice heat capacity C_{lat} decreases much faster $\sim T^3$ and does not play an important role for T$\rightarrow$ 0.

The picture is substantially different in a superconductor. The electronic heat capacity C_{el}^s does decrease with temperature and vanish in the limit T$\rightarrow$ 0; however, it does not linearly, but decays exponentially $C_{el}^s \approx \exp-\dfrac{\Delta(0)}{k_B T}$ as shown in Figure 1.7.
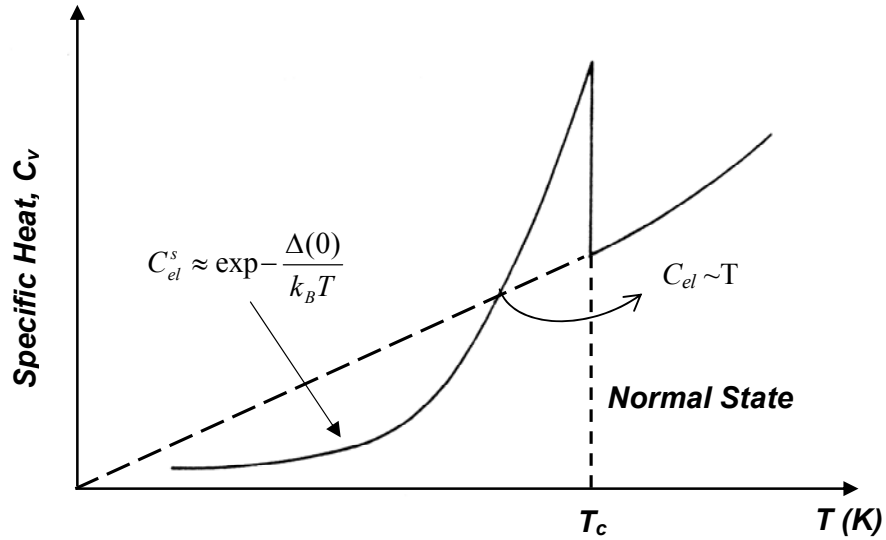
Figure 1.7: Schematic representation of the heat conductivity of a metal in the normal and the superconducting state.

The presence of energy gap and electrons bound in Cooper pairs no longer contributing to energy transport lead to the electronic heat capacity behaving different from the normal metal result, $C_{el} \sim T$. On the other hand, the temperature dependence of lattice heat capacity of superconductors C_{lat}^s in superconducting state is same as that of a metal.

The number of quasiparticle is less than the number of electrons in a normal metal and it decreases exponentially with temperature. The entropy of the system is determined by the quasiparticles in superconducting state where the entropy of normal component, i.e. of cooper pair condensate, is equal to zero. Thus, the entropy, consequently the heat capacity, decreases exponentially as $T \rightarrow 0$. The decrease in entropy between the normal state and superconducting state tells us that the superconducting state is more ordered than the normal state.

The normal-superconducting transition is a second order phase transition accompanied by a jump in the heat capacity at temperature immediately below T_c as shown in Figure 1.7. Since the lattice heat capacity does not change during the transition, it is clearly the electronic contribution that is responsible for the observed jump (Kresin and Wolf 1990)

1.3 Substrate Materials for HTS $YBa_2Cu_3O_{7-\delta}$ Thin Films

General requirements for an appropriate substrate material to produce the best quality epitaxial YBCO thin film are that chemical compatibility, lattice match, thermal expansion match, substrate surface quality, substrate homogeneity. A proper substrate material does not react chemically with YBCO. The most combinations of substrate and films will be more or less mismatched in regard to the thermal expansion. This might result in loss of adhesion or film cracking during the thermal cycling. In case of HTS materials such as YBCO, this requirement is particularly important due to the brittleness of the YBCO. An ideal substrate surface for superconducting thin film fabrication would be flat, uniform, dense and free of twins and other structural inhomogeneities. High-temperature YBCO superconducting thin films have been grown successfully on a few materials, fulfilling the above-mentioned strict requirements, such as Lanthanum Aluminate ($LaAlO_3$), Magnesium Oxide (MgO), Neodymium Gallate ($NdGaO_3$), Saphire ($Al2O3$), Strontium Titanate ($SrTiO_3$), and Yttria stabilized Zirconium Oxide ($Y_2O_3 - ZrO_3$). Knowing the above properties of these substrates, one can choose one of the substrates for optimum designs depending on the application purpose.

In this study, we used devices patterned on MgO substrates whose physical properties are given in detail in Table 1.2. Crystalline MgO has a good lattice match with YBCO to within ~ 1% and can be grown to reasonably large sizes. The thermal conductivity of MgO as shown in Table 1.2 is one order of magnitude higher than that of $LaAlO_3$, 0.32 W/Kcm (Nahum and Richards 1991a).

This is not desirable if we want a high response magnitude from the bolometer. On the other hand, having such a high conductance is good since it will dominate effects of the other thermal parameters and hence the artifacts caused by design imperfections will have minor effects. In addition, since MgO does not have twinning, the designs will be isotropic and one will not face some of the related expected results.

Substrate	MgO
Crystal Structure	Cubic
Lattice Parameter (Å)	a = 4.216
Thermal Conductivity ($WK^{-1}cm^{-1}$)	3
Specific Heat ($JK^{-1}cm^{-3}$)	0.53
Thermal Expansion Coeff. (10^{-6})	12.8
Melting Point (Celsius)	2800
Reflectance @ 850 nm (%)	3
Transmittance @ 850 nm (%)	89.5
Absorption @ 850 nm (%)	7.5

Table 1.2: Typical properties of single crystal *MgO* substrates, note that these values might vary depending on the fabrication process techniques

CHAPTER 2

BOLOMETERS

2.1 Introduction

The noun "bolometer" is a composite word of Greek origin, namely of *bole* (beam, ray) and *metron* (meter, measure). Bolometers are an instrument used to measure infrared radiation or any other form of radiant energy which can cause a change of temperature of the sensor. Quanta of infrared light are not sufficiently energetic to be detected photoelectrically so in the far infrared region the usual method of detection depend on the heating effect of radiation on an absorbing surface. The resultant temperature change in a bolometer is detected by a change of resistance. They cover a wide range of applications such as space radiometry and spectrometry, optical communication, thermal sensing, and imaging for military or biomedical purposes. They are sensitive over a wide range of wavelength from mm radiation (~meV) via infrared and visible spectrum (~eV) up to x-ray domain (~ keV) so they are potential candidates to be used for space sciences. Cosmological applications of bolometers include characterization of the cosmic microwave background and galaxy cluster surveys. Bolometers also play an important role in the observation of far infrared astronomy from low background platforms or satellites. Since their spectral sensitivity is not strong function of wavelength (or frequency), they are often used as calibration devices for other detectors. They can also be used in air surveillance, in detection of concealed weapons, and in nuclear-fusion experiments

2.2 High-T_c Superconducting Bolometers

Since the discovery of high-T_c superconductors (HTS), much attention has been focused on the application of these materials in different types of bolometers for the near and far infrared wavelength regime (Fenner et al. 1993, Richards 1994, Brasunas and Lakew 1994, Kraus 1996, Kreisler and Gaugue 2000). High temperature superconductor edge transition bolometers are one of the prominent devices that can be used to detect electromagnetic radiation over the whole spectrum from x-ray to the far infrared wavelength range. There have been several studies investigating the optical and

thermal performance of YBa$_2$Cu$_3$O$_{7-\delta}$ (YBCO) edge transition superconductive bolometers with respect to the bias temperature and the radiation modulation frequency (Nahum et al. 1991b, Aboudihab et al. 1994, Phelan 1995, Chen et al. 1997, Fardmanesh 2001, Bozbey et al. 2004). There have also been many reports on the parameters that affect the response of the bolometers. Fardmanesh et al. (1995a) have already analyzed effects of the bias current and variation of thermal conductance on the magnitude and phase of the response of the HTS edge transition bolometers. Chou et al. (1996) have focused on dependence of the photoresponse of high temperature superconducting microbridges on the surface morphology; where in their study there is no strong evidence to support this relation. Dwir et al. (1992) have reported the wavelength independent performance of the HTS bolometers from $\lambda \sim 0.6$ to 450 µm. Ivanov et al. (2002) have reported effects of electrothermal feedback on operation of high-Tc superconducting transition edge bolometers. To the best of our knowledge, there has not been a study investigating the effect of the superconducting transition width of the film on the response of the bolometers as presented in this work.

We have investigated the change in thermal parameters and the heat propagation radiation absorption mechanism, and the influence of the superconducting transition width on the response of YBCO edge transition bolometers by measuring both the phase and magnitude of the response as a function of temperature and modulation frequency.

2.1.1 Working Principle of High-T$_c$ Edge Transition Bolometers

The high-T$_c$ edge transition bolometers measure the incident radiation intensity by measuring the changes in resistance produced by heating due to the radiation absorption as shown in Figure 2.1. As the temperature of the superconducting sample is decreased, after a certain temperature value, namely the critical temperature, the resistance of the sample rapidly drops down to zero. It is known that between T$_{c\text{-onset}}$ and T$_{czero}$, resistance of the superconducting sample is extremely sensitive to changes in temperature; slight variations in temperature leads to drastic changes in resistance. This property is the key point in the operation of a superconducting edge–transition bolometer. When superconducting sample held on superconducting transition region is biased by a constant current, a very weak IR radiation that incident on the sample would change the resistance of the sample by changing its temperature as illustrated in Figure 2.2. The change in the resistance of the sample is measured with the Four–Point Probe

Method. In this measurement method, while the DC biased current is passing through the two of probes, the other two measures the voltage across the sample.

The radiation responses, defined as the voltage change caused by radiation illumination as measured between two voltages contacts when a constant current is flowing in bolometers, can be classified into two main categories: bolometric and non-bolometric response. In the first case, the temperature dependence of equilibrium properties of the superconducting YBCO thin films is used. In other words, if the voltage change is due to the thermal effect caused by radiation heating, the response is bolometric. On the other hand, if infrared response is due to another mechanism such as the interaction between the radiation and Josephson type weak links embedded in the film, it is a non-bolometric response. Bolometric response of the superconducting thin film is proportional to the dR/dT of the films whereas non-bolometric one is not as shown in Figure 2.3. In the bolometric response, the flux of photons can directly or indirectly heat the superconductor and change the temperature of the material. This change in the temperature, which can be local, will be reflected in the I-V curve characteristic of the superconductor. For this type of detection, the superconducting detector is biased with appropriate current where the temperature derivative of the resistance, dR/dT, is large. A superconducting bolometer can exhibit good performance in terms of high sensitivity and low noise at low temperatures but its sensitivity is inherently obtained by sacrificing the speed of the response. In this type of response, there is a trade-off between magnitude of response and response speed that is determined by the thermal mass and thermal conductance of the bolometer. For bolometric response, the induced voltage change, ΔV, due to a small temperature variation of the detector, ΔT, will be equal to I (dR/dT) ΔT, where I is the bias current across the detector as shown in Figure 2.2
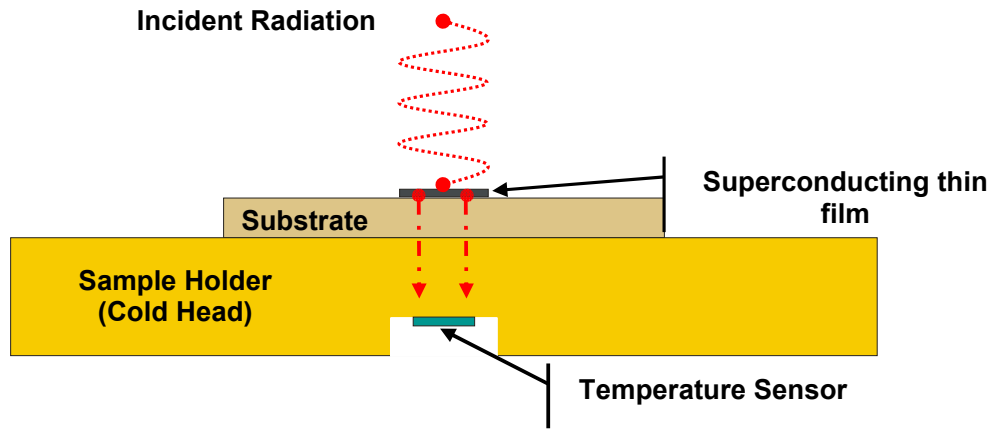
Figure 2.1: Schematic representation of working principle of the edge transition
bolometers
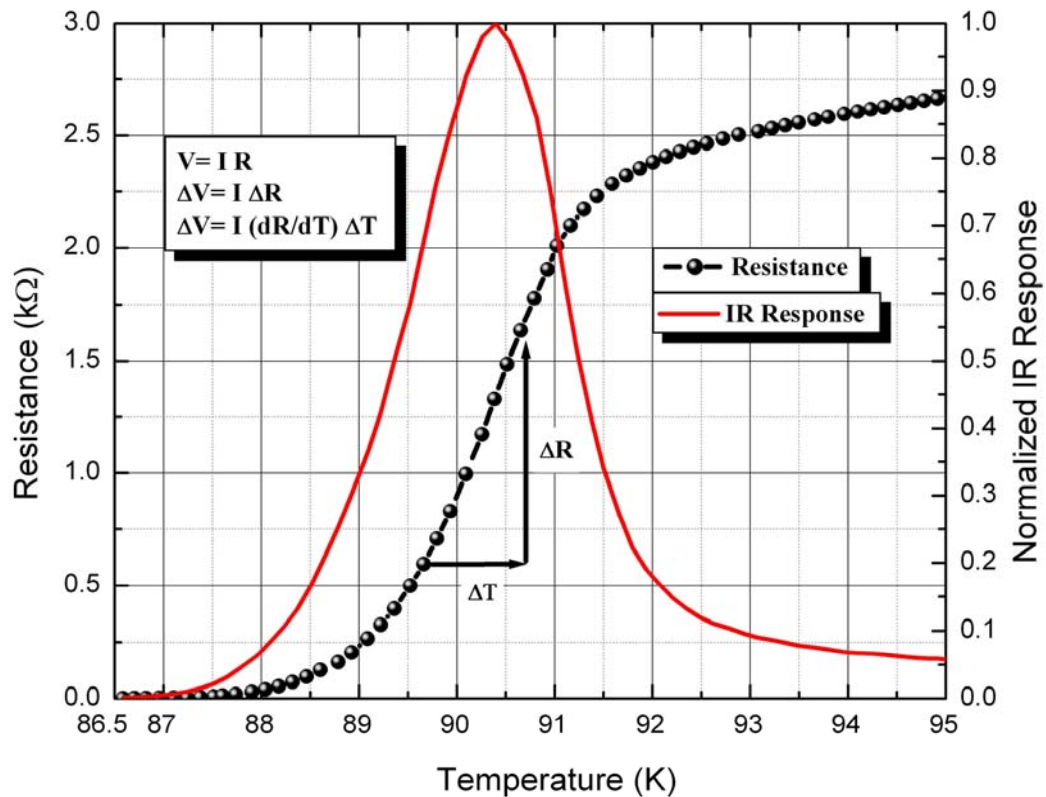
Figure 2.2: Bolometric mode of the IR detector operation. Absorbed energy produces a
temperature shift which can be observed as a change in the voltage drop
across the detector.
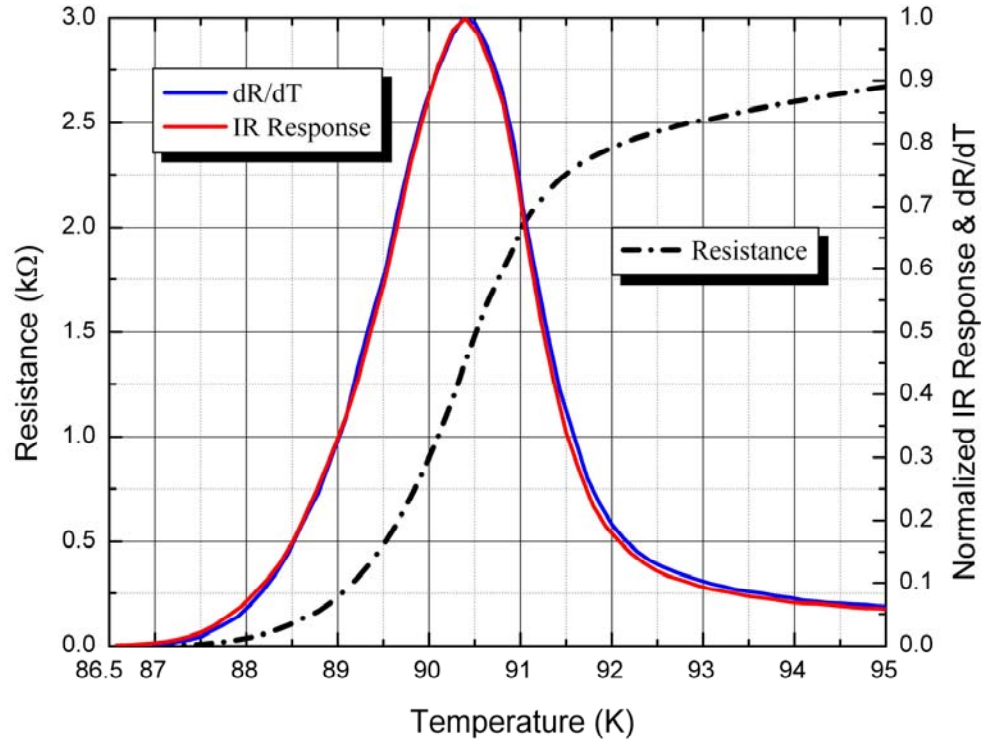
Figure 2.3: Bolometric response of the superconducting thin film is proportional to the dR/dT of the films.

2.3 Thermal Parameters of Bolometer

Before the establishing the thermal model directly, we will introduce a conceptual and terminological background in order to understand the model and the analysis.

2.3.1 Thermal Conductance, G

The thermal conductance of a bolometer is defined as the total heat conduction from the bolometer to its environment per degree of temperature change.

$$G = \frac{P_{in}}{\Delta T} \tag{2.1}$$

where ΔT is the difference between the temperature of the bolometer and its environment and P_{in} is the power given to the bolometer.

The measurement of G is basically based on the joule heating effect that creates a temperature gradient (ΔT) for an input power of $I^2 R$ between the film and cold head. There are many measurement methods of the thermal conductance of the bolometers. In one of the methods, we apply a constant bias current to the bolometer and increment the holder temperature from $T_{c\text{-zero}}$ to higher values while measuring the IR response. Then, we repeat this for different bias currents. For higher bias currents we observe that the response shifts to the lower temperatures due to the joule heating. Therefore, we can calculate the thermal conductance, G, by using temperature shift, ΔT, the resistance value, R, at that point and bias current, I as shown in Figure 2.4 (Bozbey 2003).
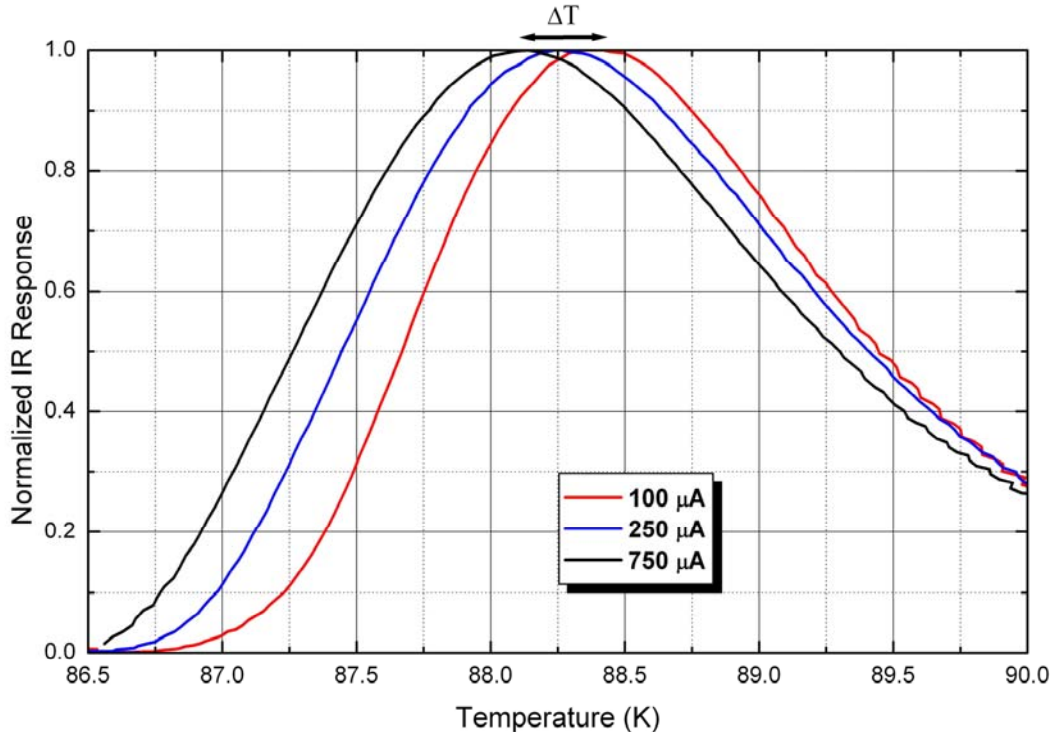
Figure 2.4: Normalized IR response versus temperature for different bias current under 20 Hz modulation frequency.

2.3.2 Thermal Diffusion Length, L_f

The thermal diffusion length, L_f, represents the characteristics penetration depth of the temperature variation into the substrate and is given by;

$$L_f = \sqrt{\frac{D}{\pi f}} \tag{2.2}$$

where f is the modulation frequency, $D = \dfrac{k_s}{c_s}$ is the thermal diffusivity of the substrate and k_s and c_s are the thermal conductivity and the heat capacity of substrate material, respectively. The thermal diffusivity describes the rate at which heat diffuse through a body. It increases with increasing thermal conductivity since heat will able to conduct across the body quickly. The thermal diffusivity decreases with increasing thermal capacity of the substrate because heat is preferentially stored as internal energy within the body instead of being conducted trough it.

Knee frequency, f_L, is a frequency that thermal diffusion length becomes equal to the thickness of the substrate, L.

For the MgO substrate;

$$D = \frac{k_s}{c_s} = \frac{3}{0.53} = 5.66 \ cm^2 / s \tag{2.3}$$

$$f_L = \frac{D}{\pi L^2} = \frac{5.66}{\pi (0.05)^2} = 720 \ Hz \quad where \ L_f = L \tag{2.4}$$

The values of k_s, c_s, and the calculated frequency of the knee point, f_L, of the three different substrates used in this work are given in Table 2.1 (Fardmanesh et al. 1999).

Table 2.1: Thermal characteristics of single crystal substrates

Substrate	Thermal Conductivity k_s (W/K-cm)	Heat Capacity c_s (J/K-cm^3)	Thermal Diffusivity D (cm^2/s)	Knee Frequency f_L@ L=0.05cm (Hz)	Knee Frequency f_L@ L=0.1cm (Hz)
MgO	3	0.53	5.66	720	180
LaAlO$_3$	0.32	0.59	0.55	70	17.5
SrTiO$_3$	0.052	0.43	0.12	15.4	3.85

2.4 The Thermal Models of Bolometer

In order to understand the relation between the magnitude (and phase) of the response and thermal parameters of the bolometers, which are usually frequency dependent, we need some kind of thermal model that can predict the effect of the different parameters related to the bolometers.

Before establishing the thermal model, we can make an analogy between thermal parameters of the device and electrical parameters of a circuit as given in Table 2.2. According to this analogy, the heat flow is considered as the current flow resulting in the heat to be charge and the temperature being voltage in the equivalent circuit. Once these substitutions are made, the electrical formulas and intuition can be applied to the thermal problems.

Table 2.2: Electrical analogous of the thermal parameters used in modeling the heat
propagation

Thermal Parameter	Electrical Analog
Heat Energy (J)	Charge (C)
Heat Flow (W)	Current (A)
Temperature (K)	Voltage (V)
Thermal Impedance (K/W)	Impedance (V/A, Ω)
Thermal Conductance (W/K)	Conductance (A/V, 1/Ω)
Heat Capacity (J/K)	Capacitance (C/V)

2.4.1 Simple RC Model
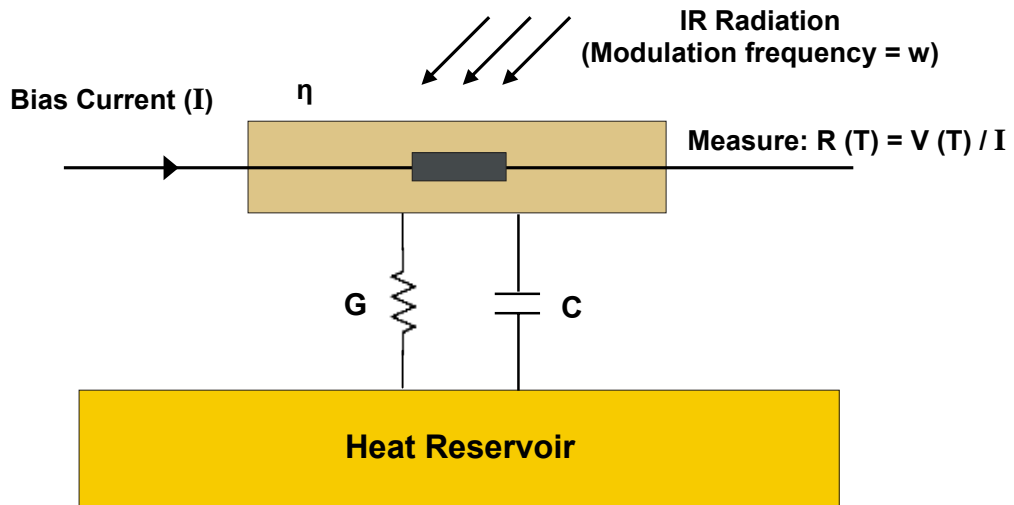
Figure 2.5:   Schematic of the simple RC model with thermal conductance *G* and thermal
capacitance *C*

Traditional classic modelling suggests the following equivalent circuit of the Figure 2.5 as a thermal model for thermal detectors, especially bolometers. There is also a rather complex thermal model used in this study for the holder configuration as illustrated in Figure 2.6. However, the operation and response of a bolometer can most easily be understood with a simple RC model shown in Figure 2.5.

The magnitude of the bolometric response can easily be calculated with a simple RC-model resulting in following expression (Richards et al. 1989, Nahum et al. 1991c, Fardmanesh et al. 1995b):

$$r = \left(\frac{\eta I}{G + j\omega C} \right) \frac{dR}{dT} \ , \tag{2.5}$$

where r is the frequency-dependent responsivity, I is the dc bias current, η is the absorption coefficient, $\omega = 2\pi f$ with f being the modulation frequency, dR/dT is the slope of the resistance versus temperature curve at the bias temperature, and G and C are the total thermal conductance and the heat capacity of the bolometer, respectively. According to Equation (2.5), the temperature-dependent phase of the response can be obtained from

$$\tan \theta = -\frac{\omega C}{G} \tag{2.6}$$

The basic RC model is found to be useful as a complete model in the low frequency ranges in which the thermal diffusion length into the substrate is much larger than the substrate thickness.

2.4.2 Advanced Thermal Model
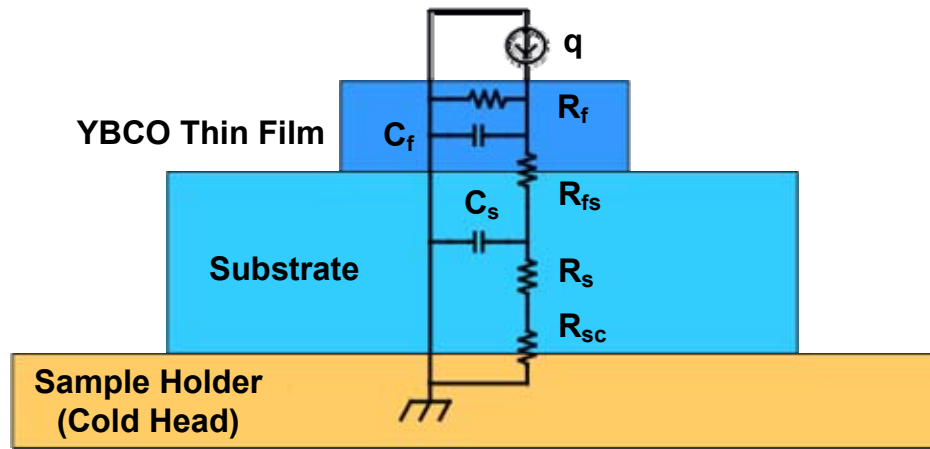
Figure 2.6: Electrical analog of the one dimensional thermal model. The physical dimensions are not to scale.

Bozbey et al. (2003) have established a one-dimensional thermal model associated to the characterization setup illustrated in Figure 2.6. In this model, q is the absorbed radiation intensity at the surface of the sample, R_f is the film lateral thermal resistance due to conduction through the YBCO to the contact areas, C_f is the heat capacity of the film, R_{fs} and R_{sc} are thermal boundary resistances values at the film-substrate and substrate- cold head interfaces, respectively, and R_s and C_s are the thermal resistance and heat capacity of the substrate material, respectively. While the R_f, C_f, R_{fs}, and R_{sc} parameters can be used as a lumped circuit element in the model, the R_s and C_s cannot be used. Thus, in order to find the thermal impedance seen from the surface of the film, we should find the thermal impedance of the substrate. We can do this by using the analogy between a transmission line and the substrate. If we divide the substrate into infinitesimally small segments, one of which is shown in Figure 2.7, a substrate segment of thickness Δx can be modeled with a simple RC circuit. The resistance of the segment is calculated by $r(x)\Delta x$ where $r(x)$ is the unit length resistance at position x and the capacitance is calculated with $c(x)\Delta x$ where $c(x)$ is the unit length capacitance at position x.
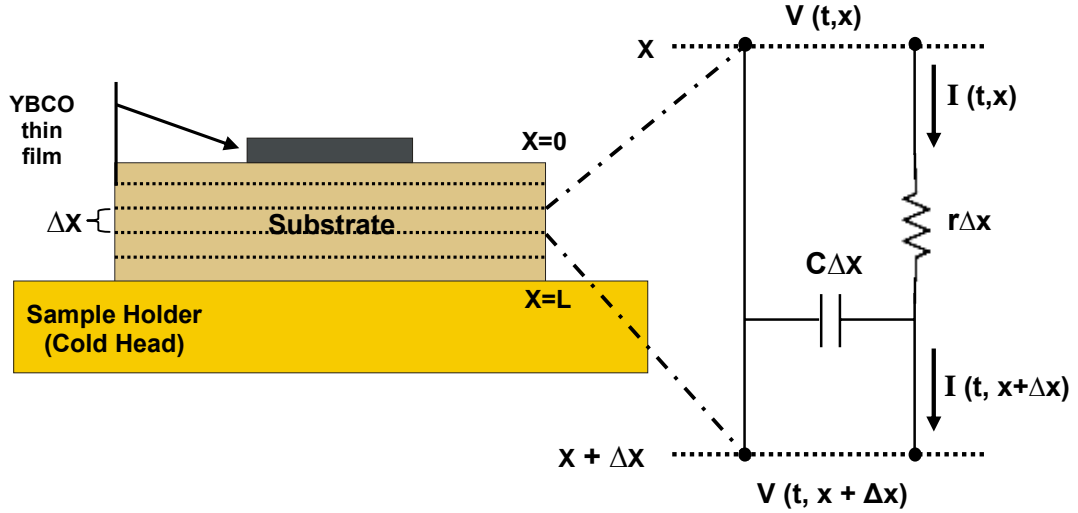
Figure 2.7: Circuit analog of a substrate segment, Δx. $r\Delta x$ and $c\Delta x$ are segment resistance and capacitance. r and c is the unit length resistance and capacitance respectively. The physical dimensions are not to scale.

By using Kirchoff's voltage and current laws, the equilibrium equations of the circuits are found as

$$v(t, x + \Delta x) - v(t, x) = -r(x) \; \Delta x \; i(t, x + \Delta x) \qquad (2.7)$$

$$i(t, x + \Delta x) - i(t, x) = -c(x)\Delta x \frac{\partial v(t, x + \Delta x)}{\partial t} \qquad (2.8)$$

when we divide both sides of the equations 2.7 and 2.8 to Δx, we can get

$$\frac{v(t, x + \Delta x) - v(t, x)}{\Delta x} = -r(x) \; i(t, x + \Delta x) \qquad (2.9)$$

$$\frac{i(t, x + \Delta x) - i(t, x)}{\Delta x} = -c(x) \frac{\partial v(t, x + \Delta x)}{\partial t} \qquad (2.10)$$

In the limit $\Delta x \to 0$, we obtain the following partial differential equations,

$$\frac{\partial v(t, x)}{\partial x} = -r(x) \; i(t, x) \qquad (2.11)$$

29

$$\frac{\partial i(t,x)}{\partial x} = -c(x)\frac{\partial v(t,x)}{\partial t} \qquad (2.12)$$

If we take the Fourier transforms,

$$\frac{\partial V(w,x)}{\partial x} = -r(x)I(w,x) \qquad (2.13)$$

$$\frac{\partial I(w,x)}{\partial x} = -jwc(x)V(w,x) \qquad (2.14)$$

When we take the derivative of the above equations, we obtain

$$\frac{\partial^2 V(w,x)}{\partial x^2} = -r(x)\frac{\partial I(w,x)}{\partial x} - I(w,x)\frac{dr(x)}{dx} \qquad (2.15)$$

$$\frac{\partial^2 I(w,x)}{\partial x^2} = -jwc(x)\frac{\partial V(w,x)}{\partial x} - jwV(w,x)\frac{dc(x)}{dx} \qquad (2.16)$$

Substituting 2.13 and 2.14 into 2.15 and 2.16, we get following equations;

$$\frac{\partial^2 V(w,x)}{\partial x^2} = jwr(x)c(x)V(w,x) + \frac{1}{r(x)}\frac{\partial V(w,x)}{\partial x}\frac{dr(x)}{dx} \qquad (2.17)$$

$$\frac{\partial^2 I(w,x)}{\partial x^2} = jwc(x)r(x)I(w,x) + \frac{1}{c(x)}\frac{\partial I(w,x)}{\partial x}\frac{dc(x)}{dx} \qquad (2.18)$$

These equations have been solved by using Mathematica for arbitrary *r(x)* and *c(x)*.
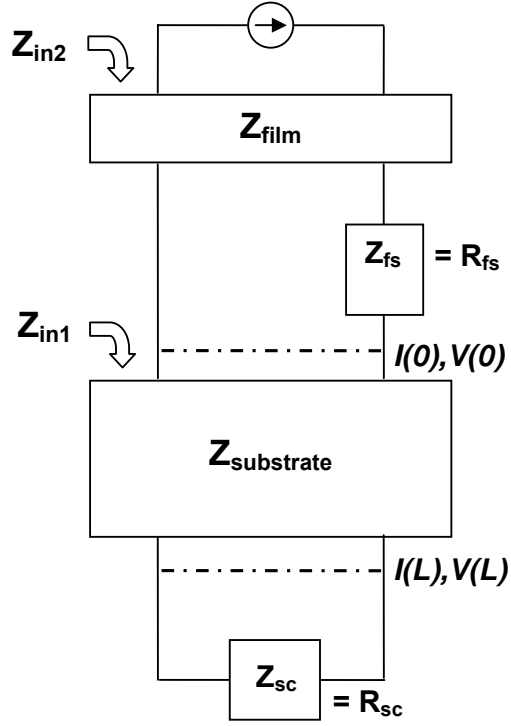
Figure 2.8: Impedance representation of the holder configuration

From the basic RC circuit, impedance of the superconducting YBCO thin film can be calculated as follows;

$$\frac{1}{Z_{film}} = \frac{1}{R_f} + jwC_f \tag{2.19}$$

$$Z_{film} = \frac{R_f}{1 + jwC_f R_f} \tag{2.20}$$

As shown in Figure 2.8, there are two input impedances determined as

$$Z_{in1} = Z_{substrate} \oplus Z_{sc}(R_{sc}) \tag{2.21}$$

$$Z_{in2} = Z_{film} \oplus Z_{fs}(R_{fs}) \oplus Z_{in1} \tag{2.22}$$
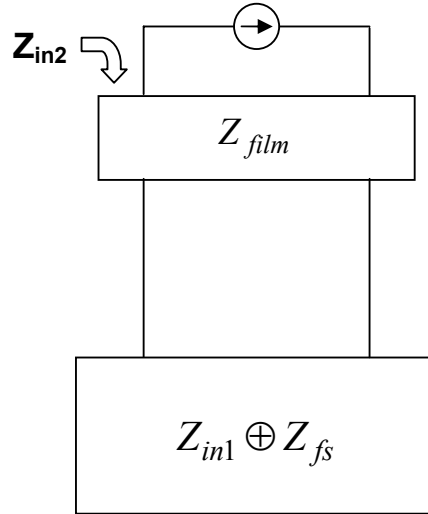
Figure 2.9:   Schematic of impedance representation of the holder configuration to find Z_{in2}

We can calculate Z_{in2} from the Figure 2.9

$$\frac{1}{Z_{in2}} = \frac{1}{Z_{film}} + \frac{1}{Z_{in1} + Z_{fs}} \tag{2.23}$$

$$Z_{in2} = \frac{Z_{film}\left(R_{fs} + Z_{in1}\right)}{Z_{film} + R_{fs} + Z_{in1}} \quad \text{where} \quad Z_{fs} = R_{fs} \tag{2.24}$$
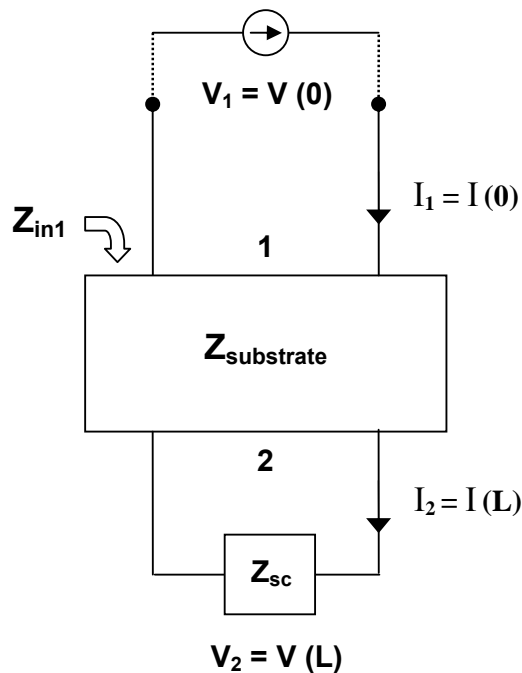
Figure 2.10: A two-port with two current sources terminated by Z_{sc}

The impedance matrix of the substrate is obtained by writing the two loop equations using Kircohoff's voltage law as shown in Figure 2.10,

$$V_1 - z_{11}I_1 - z_{12}I_2 = 0 \tag{2.25}$$

$$V_2 - z_{21}I_1 - z_{22}I_2 = 0 \tag{2.26}$$

$$\begin{pmatrix} V_1 \\ V_2 \end{pmatrix} = \begin{pmatrix} z_{11} & z_{12} \\ z_{21} & z_{22} \end{pmatrix} \begin{pmatrix} I_1 \\ I_2 \end{pmatrix} \quad \text{where} \quad Z_{sub} = \begin{pmatrix} z_{11} & z_{12} \\ z_{21} & z_{22} \end{pmatrix} \tag{2.27}$$

We can calculate the impedance Z_{in1} as in equation 2.28 from the two port model terminated by Z_{sc} (Chua et al. 1987).

$$Z_{in1} = \frac{V_1}{I_1} = \frac{z_{11}I_1 + z_{12}I_2}{I_1} = z_{11} + \frac{z_{12}I_2}{I_1} \tag{2.28}$$

$$V_2 = I_2 Z_{sc} = I_2 R_{sc} \tag{2.29}$$

By substituting equation 2.29 into 2.26, we can obtain the expression as follows

$$I_2 R_{sc} - z_{21}I_1 - z_{22}I_2 = 0 \tag{2.30}$$

Form the equation 2.30, we get a relation between I_2 and I_1

$$\frac{I_2}{I_1} = \frac{z_{21}}{R_{sc} - z_{22}} \tag{2.31}$$

By substituting equation 2.31 into 2.28, we can calculate Z_{in1}

$$Z_{in1} = z_{11} + \frac{z_{12}z_{21}}{R_{sc} - z_{22}} \tag{2.32}$$

For large area bolometer, the area of the superconducting pattern of the samples is large with respect to the substrate thickness. Thus, we can use uniletarel heat propagation and consider the propagation area equal to the film area throughout the

33

substrate. Then we obtain $r(x) = r_s / A = 1/(k_s * A)$ and $c(x) = c_s * A$. For these values of $c(x)$ and $r(x)$, we can rewrite the equations 2.17 and 2.18 as follows;

$$\frac{\partial^2 V(w,x)}{\partial x^2} - \gamma^2 V(w,x) = 0 \tag{2.33}$$

$$\frac{\partial^2 I(w,x)}{\partial x^2} - \gamma^2 I(w,x) = 0 \tag{2.34}$$

where $\gamma = \sqrt{jw\dfrac{c_s}{k_s}}$ is the characteristic thermal impedance of the substrate material.

$$z_{11} = \frac{V_1}{I_1}\bigg|_{I_2=0} ; \quad z_{12} = \frac{V_1}{I_2}\bigg|_{I_1=0} ; \quad z_{22} = \frac{V_2}{I_2}\bigg|_{I_1=0} ; \quad z_{21} = \frac{V_2}{I_1}\bigg|_{I_2=0} \tag{2.35}$$

where $V(0) = V_1$, $I(0) = I_1$, $V(L) = V_2$, and $I(L) = I_2$ as shown in Figure 2.8.

By using the above one dimensional differential equations and boundary conditions as in 2.35, we can obtain the substrate matrix Z_{sub} as follows

$$Z_{sub} = \frac{1}{\sqrt{jc_s k_s w}}\begin{pmatrix} \coth(\gamma L) & -\csc h(\gamma L) \\ \csc h(\gamma L) & -\coth(\gamma L) \end{pmatrix} \tag{2.36}$$

Z_{in1} and Z_{in2} are found by using equations 2.24 and 2.32 as follows

$$Z_{in1} = \frac{e^{\gamma L} + \Gamma e^{-\gamma L}}{e^{\gamma L} - \Gamma e^{-\gamma L}} \sqrt{\frac{1}{jc_s k_s w}} \tag{2.37}$$

$$Z_{in2} = \frac{\dfrac{e^{\gamma L} + \Gamma e^{-\gamma L}}{e^{\gamma L} - \Gamma e^{-\gamma L}} \sqrt{\dfrac{1}{jc_s k_s w}} + R_{fs}}{\dfrac{e^{\gamma L} + \Gamma e^{-\gamma L}}{e^{\gamma L} - \Gamma e^{-\gamma L}} \sqrt{\dfrac{jw}{c_s k_s}} C_f + 1 + jwC_f R_{fs}} \tag{2.38}$$

34

where
$$\Gamma = \frac{R_{sc} - \sqrt{\dfrac{1}{jc_s k_s w}}}{R_{sc} + \sqrt{\dfrac{1}{jc_s k_s w}}}$$
(3.39)

Finally, the temperature variation caused by the radiation absorption in the superconductive film of the samples was obtained for all considered frequency ranges to find the voltage response to the modulated radiation intensities by using the expression, $\Delta T = q * Z_{in.2}$;

$$\Delta T = q \left(\frac{\dfrac{e^{\gamma L} + \Gamma e^{-\gamma L}}{e^{\gamma L} - \Gamma e^{-\gamma L}} \sqrt{\dfrac{1}{jc_s k_s w}} + R_{fs}}{\dfrac{e^{\gamma L} + \Gamma e^{-\gamma L}}{e^{\gamma L} - \Gamma e^{-\gamma L}} \sqrt{\dfrac{jw}{c_s k_s}} C_f + 1 + jwC_f R_{fs}} \right)$$
(2.40)

The obtained solution of equation 2.40 is up to frequencies at which the thermal diffusion length into the superconducting film becomes smaller or comparable with the thickness of the film. At dc and low frequencies, below the knee frequency, the thermal diffusion length into the substrate becomes larger than the substrate thickness and the phonons emitted by the superconducting film into the substrate will reach the substrate-cold head boundary ($L_f \gg L$). The value of the total thermal conductance of the sample is found to be determined by the substrate-cold head interface conductance ($G \approx G_{sc}$). The heat capacity of the film, C_f, and thermal boundary resistance of the film-substrate interface, R_{fs}, can be ignored compared to those of the substrate. Thus, at this frequency regime, the dominator of temperature variation expression 2.40 will approach 1 and R_{fs} will become negligible compared with the first term of the numerator and then the temperature variation at the surface of the substrate can be written as

$$\Delta T = q \left(\frac{e^{\gamma L} + \Gamma e^{-\gamma L}}{e^{\gamma L} - \Gamma e^{-\gamma L}} \sqrt{\frac{1}{jc_s k_s w}} \right)$$
(2.41)

35

For a small area pattern, the unilateral propagation approximation can not be used since the film pattern area is much smaller than the substrate thickness. The heat propagation path has not yet been found so the temperature variation in the superconductive samples was not calculated.

CHAPTER 3

FABRICATION AND CHARACTERIZATION

3.1 Fabrication

The samples were made of YBCO thin films of 200 nm thickness that were deposited 'in situ' by using DC inverted cylindrical magnetron sputtering technique on 0.5-1 mm thick MgO (100) substrates. We patterned small and large area meander designs and microbridges using the standard photolithography process and chemical etching. The large area meanders with 50 and 100 μm wide resulted in 1.7 and 6 mm^2 effective areas and the microbridge and the small area meanders with 12 and 10 µm wide resulted in 0.003 and 0.012 mm^2 effective areas respectively. We coated the contact pads of YBCO patterns with ~ 80 nm thick gold layer and contacted copper wires with silver epoxy resulting in very low resistance (< 0.1 Ω) contacts at low temperatures. We attached the devices to the cold head with a very thin layer of vacuum grease which was applied to the back side of the substrate to improve the thermal contact between the substrate and cold-head. More details on the deposition parameters, the properties of the films, and the fabrication steps are given in the following sections.

3.1.1 Overview of Thin Film Deposition Technologies

A large variety of thin films are used in today's industry for the fabrication of various microelectronic, optical, and bioengineering devices. There exist many different deposition technologies for the formation of such thin films on a substrate. Thin film deposition methods refer to processes used for the formation of layers in the thickness range of a few nanometers to about 10 micrometers. Thin films are normally prepared by condensation of atoms or molecules from the vapor phase. Thin film deposition techniques can be divided into three groups:

- *Chemical Vapor Deposition (CVD)*: Solid films are formed on a substrate by the chemical reaction of vapor phase chemicals that contain the required constituents.

- *Liquid Phase Chemical Formation (LPCF)*: This involves coating of a substrate with a liquid which is then dried to form a solid thin film.

- *Physical Vapor Deposition (PVD)*: Species of the thin film are dislodged from a source to form a vapor which is transported across a reduced pressure region to the substrate where it condensed to form the thin film. PVD can be divided into three major sub-classes: evaporating technology, molecular beam epitaxy (MBE) and sputtering technology (Schuegraf 1988, Seshan 2002). The thin superconducting $YBa_2Cu_3O_{7-\delta}$ films used in this thesis have been mainly deposited by using "DC inverted cylindrical magnetron sputtering" technique, so the working principle of this technique will described in the rest of this section.

Sputter deposition technique is one of the frequently used techniques for deposition of High-T_c superconducting (HTSC) thin films. Sputtering is a process in which atoms are ejected from the surface of a target when that surface is struck by sufficiently energetic ions. From this definition, sputtering can be considered as an etching process and is used for surface cleaning. Since sputtering removes and transports the target material, it is also used as a method of film deposition. There are numerous variants of sputter deposition in use today. They can be classified as DC diode sputtering, RF diode sputtering, Magnetron Sputtering, and Ion beam sputtering. Sputter deposition may be carried out in a variety of systems, which may differ in the sputtering configuration, geometry, target type, substrate position, and gas type and pressure. The difference between systems do not change the basic sputtering process itself, that is, all processes rely upon the ejection of atoms from a target due to an energetic ion impact.

Magnetron sputtering is a sputtering process in which plasma is confined by a magnetic field produced by magnetrons behind the target. There are several types of magnetrons for practical application. The most configurations are planar and cylindrical magnetron sputtering. In Planar magnetron electrode configuration the target surface is planar, and the magnetic field is created by permanent magnets behind target whereas in cylindrical magnetron system has a cylindrical shaped target and an axial magnetic field.

When a critical threshold voltage is reached the working gas breaks down to conduct electricity and plasma is generated close the target in partial passive source gas (i.e. Argon) in the chamber. When the accelerated Ar^+ ion bombards a target surface, the following possible events may occur as shown Figure 2.1.:

- The ion may be implanted in the target.

- The bombarding ion may be reflected and neutralized in the process if it does not have enough energy to imbed itself in the target. The lower mass of the incident ion relative to the target atoms is the higher the probability of reflection.

- The impact of a particle with a target surface may lead to structural rearrangements such as the introduction of interstitials or vacancies. It may also introduce lattice defects such as stoichiometry modifications.

- The ion impact may set up series of collision between atoms of the target, leading to the ejection of one of the target atoms. This injection process is known as sputtering.

- The impact of the ions may cause the target to emit an electron called the secondary electron.

Incident Argon Ion (Ar$^+$)   **Reflected Argon Atom (Ar)**   **Ar$^+$**   **Secondary Electron**   **Sputtered Atom**

Target Surface

Structural Rearrangement

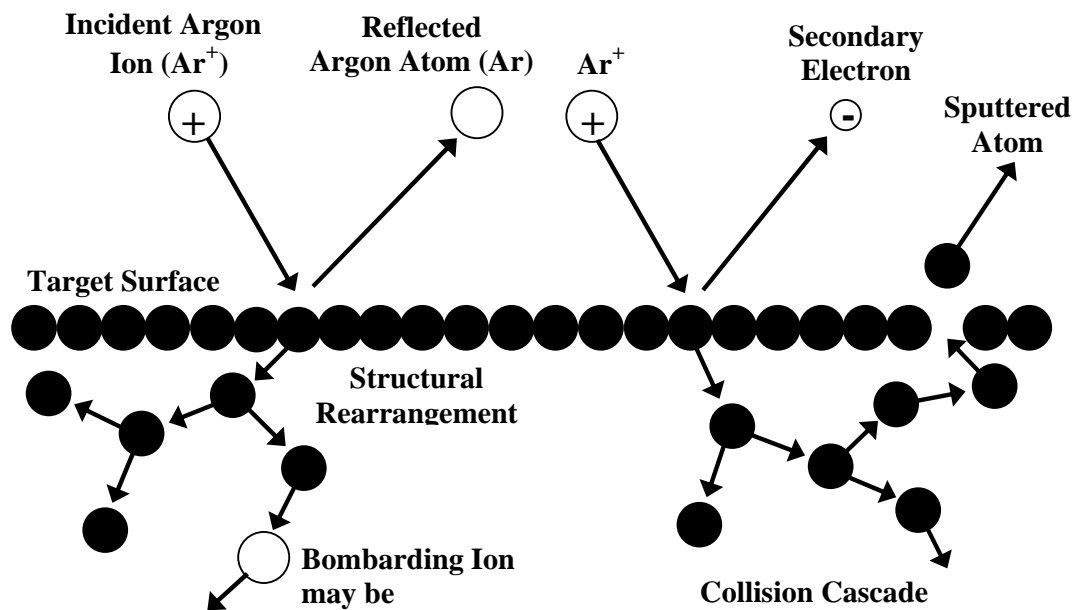**Bombarding Ion may be**

Collision Cascade

Figure 3.1:   Interactions due to ion bombardment. Sputtering of a target atom is just one of the possible results of ion bombardment. Aside from sputtering the second important process is the emission of secondary electrons from the target surface. The other possibilities are summarized above.

After the ejection of the secondary electrons from the target, they are accelerated toward to substrate. As they propagate, collisions occur with working gas atoms (i.e. Ar atoms) resulting in their ionization which and replenishment of the Ar^+ ion necessary for sputtering and to produce more secondary electrons to sustain the discharge. Magnetron sputtering uses strong magnetic fields generated by the magnets transverse to the electric field to concentrate the plasma near the target surface to increase the deposition rate. Secondary electrons are trapped near the target surface by combination of the magnetic field and electric fields, and continue to move with a cyclodial motion until they collide with an Ar atom. This increases the path length in the plasma, and increases the probability of collisions with the background gas. Since the impact efficiency of the available electrons with the working gas is increased, it is possible to sputter at low pressures than those used for either DC or RF diode sputtering. The lower pressure in the chamber helps producing high-purity thin films. Moreover, confining the electrons with cyclodial motion in the region of the target reduces the amount of electron bombardment of the substrate and walls of the chamber and thus such trapped secondary electrons do not contribute to increase substrate temperature and radiation damage. This causes the magnetron sputtering system to be able to coat heat-sensitive substrates. In diode sputtering, in contrast to magnetron sputtering, not all of the electrons emitted from the target surface contribute to the ionized plasma glow area and the wasted electrons fly around the chamber causing radiation and other problems, for example, the heating of the target and substrate (Kiyokata and Hayakawa 1992, Mattox 1998, Rossnagel et al. 1990).

3.1.2 YBCO Thin Film Deposition

$YBa_2Cu_3O_{7-\delta}$ (YBCO) thin films used in this experiment were deposited by DC inverted cylindrical magnetron sputtering (ICMS) technique on <100>-oriented and 10x10x1-0.5 mm^3 sized single crystal MgO substrates. The magnetron sputtering system used in this work is shown in Figure 3.2.

Before the deposition process, the cleaning of the substrate surfaces within the appropriate solutions exerts a decisive influence on the superconducting thin film growth and adhesion. A thoroughly cleaned substrate is a prerequisite for the preparation of films with reproducible properties. The aim of the cleaning process is to remove contaminants such as residues from manufacturing and packaging, lint, fingerprints, oil, and airborne particulate matter from the surface of the substrate. In this

study, the MgO substrates were cleaned with ultrasonic cleaner in acetone for half an hour and then subsequently in isopropyl alcohol for half an hour. The substrates attached to the Teflon holder were placed into the ultrasonic bath as their polished surfaced facing down to the path liquid with an angle of 45°. Then the ultrasonic cleaner was started with adjusting the temperature of the water inside to 30 °C. Finally, the ultrasonic cleaned substrates were dried with argon gas. After the cleaning process, the cleaned MgO substrate was glued to the centre of substrate holder of the sputtering system by using fast-drying silver paste. There is no need to apply high pressure on the substrate surface since the silver paste easily spreads to the edges of the substrate. The target–substrate distance was optimized at 35 mm. The deposition chamber was slowly evacuated to $2x10^{-3}$ mbar with a rotary pump using a special oil resistant to oxygen gas and then the Argon partial pressure was adjusted to 0.5 mbar by means of needle-valve. The target was presputtered in an Argon atmosphere for 50 minutes at a power of 45 W during which the temperature of the sample holder was increased up to the deposition temperature of 800°C. The pre-sputtering process results in removing any contamination on the surface of the YBCO target. At 800°C, the oxygen gas was introduced into the chamber to attain the partial pressure of oxygen of 0.1 mbar and finally the total pressure inside the chamber was $P_{Ar}+P_{O2} = 0.6$ mbar. The thin films deposition process was started with under these fixed deposition conditions such as; the partial pressures of Ar and O_2 gases of 0.5 mbar and 0.1 mbar, respectively, plasma power of 45 W, and substrate temperature of 800 °C. The resulting deposition rate of the YBCO thin film was about 1.3nm/min. After the deposition, pure oxygen was injected into the deposition chamber with the pressure of 1 mbar while the temperature of the sample holder was fixed at 800°C for 10 minutes and then it was decreased to 600 °C at a rate of 20°C/min. At the beginning of the cooling process from 800 to 600 °C, oxygen pressure was raised up to 700 mbar and the samples were held at 600 °C for 20 minutes, then the temperature was allowed to fall down to room temperature at a rate of 30°C/min. The deposition recipe for YBCO thin films is illustrated in Figure 3.3. We obtained c-axis epitaxial YBCO thin films using the above optimum deposition parameters. In order to produce films differing in their quality, we placed one substrate close to outer rim of the sputtering plasma cone on the substrate holder which resulted in obtaining a film with high density of the precipitates on its surface while keeping the other substrate at the centre of the holder coinciding with the symmetry axis of the same plasma producing a film with much less concentration of precipitates.
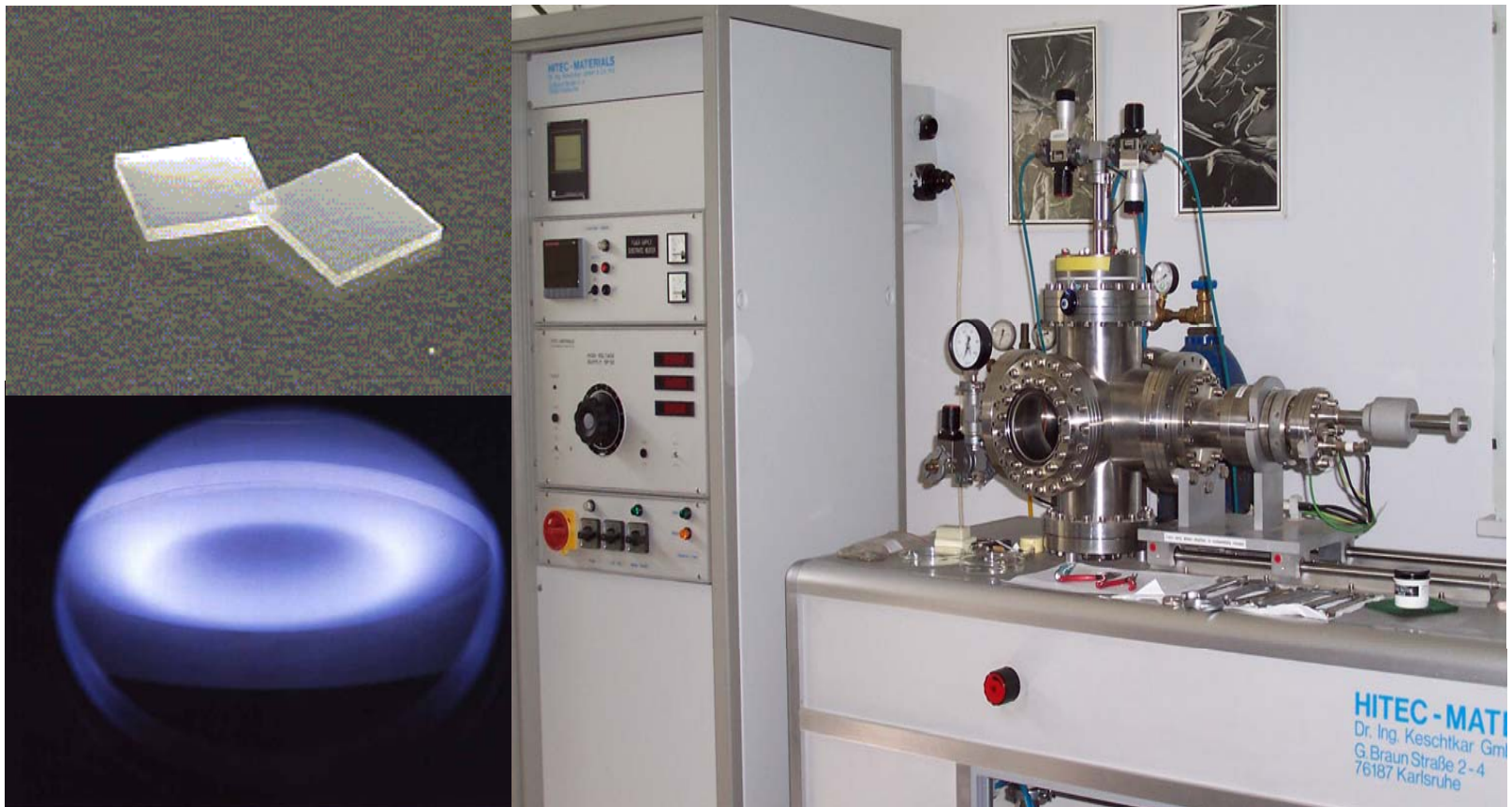
Figure 3.2: DC inverted cylindrical magnetron sputtering (ICMS) system.

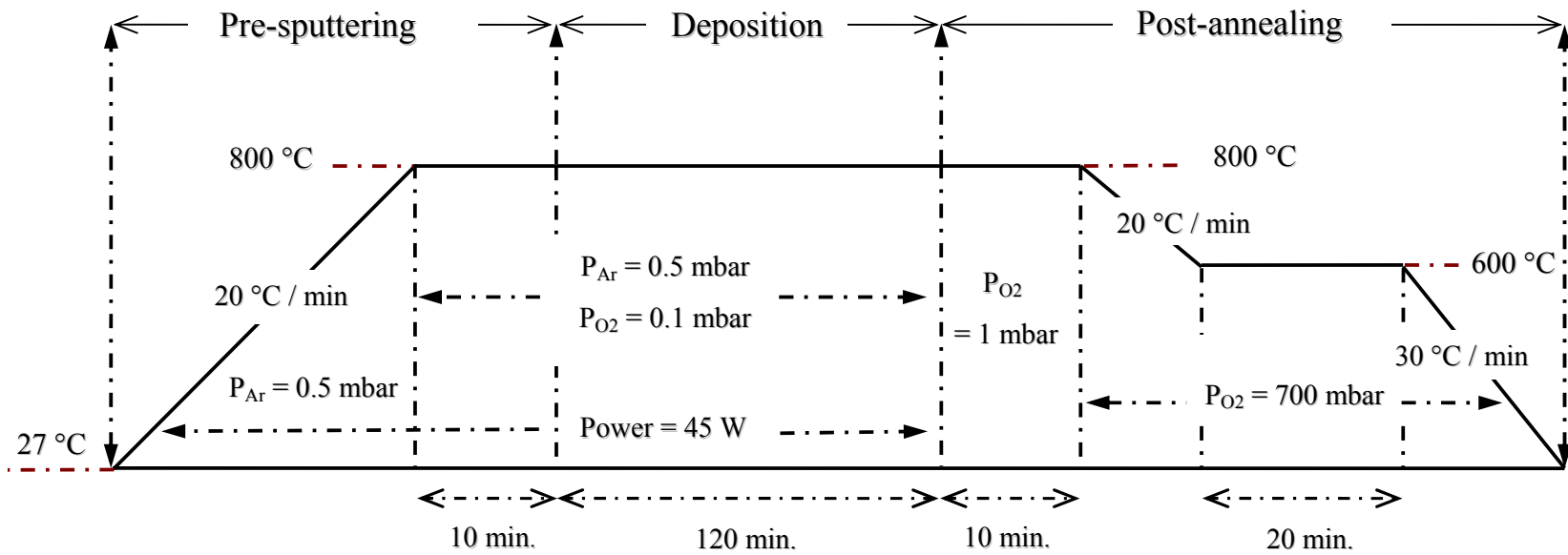# Deposition Recipe of YBCO Thin Films on MgO Substrates

Figure 3.3: The deposition recipe of YBCO thin films on MgO substrates

3.1.3 Patterning

We patterned small and large area meander designs and microbridges using the standard photolithography process and wet etching as illustrated in Figure 2.4. In this study, the steps which have been followed to pattern the bolometers on superconducting thin films are;

- The YBCO superconducting thin film was chemically cleaned to remove particulate matter on the surface as well as any traces of organic, ionic, and metallic impurities by using Acetone and Isopropyl Alcohol with ultrasonic agitation for one minute respectively. Typical contaminants that must be removed prior to photoresist coating are atmospheric dust which could be minimized by good clean room practice, lint from wipers which should be minimized by using lint-free wipers, and oil.

- The film was coated with positive AZ5214 photoresist material by using an eyedropper. Uniform, defect free photoresist with correct thickness is coated with proper adherence on the thin film by spin coating technique. Spin-coating consists of dispensing the resist solution over the film surface and rapidly spinning the sample until it becomes dry. Spin-coating process was conducted at spin speeds of 6000 rpm for duration of 40 seconds.

- Resist coating was followed by a soft bake which has been done to drive away the solvent from the spun-on resist, to improve the adhesion of the resist to the thin film, and to anneal the shear stresses introduced during the spin-coating. Soft baking has been performed using hot plate. Soft-bake hot plate must provide well-controlled and uniformly distributed temperatures and a bake environment that possesses a high degree of cleanliness. The sample with photoresist was soft backed for 3 minutes at 90°C.

- After the sample was coated with photoresist and subjected to soft baking, it has to undergo exposure to Ultra-Violet (UV) radiation that would produce the pattern image on the resist for duration of 140 seconds. The pattern was formed on the sample using a mask aligner with an appropriate glass mask, which defines which areas of the resist surface will be exposed to radiation and those that will be covered. The chemical properties of the resist regions struck by radiation change in a manner that depends on the type of resist used. Irradiated regions of positive photoresist will become more soluble in the developer, so positive resists form a positive image of the mask on the sample. Negative resists form a negative image of the mask on the sample because the exposed regions become less soluble in the developer.

- The sample was developed by using developer - distilled water mixture. The type of photoresist chosen determines the type of developer solution used. Development, which is the process step that follows resist exposure, is done to leave behind the correct resist pattern on the sample which will serve as the physical mask that covers areas on the sample that need to be protected from chemical attack during subsequent etching, implantation, lift-off, and the like. The development process involves chemical reactions wherein unprotected parts of the resist get dissolved in the developer. A good development process has a short duration (less than a minute), results in minimum pattern distortion or swelling, keeps the original film thickness of protected areas intact, and recreates the intended pattern faithfully.

- Development was followed by thorough rinsing with DI-water and drying with nitrogen gas to ensure that the development action will not continue after the developer has been removed from the sample surface.

- After the development process, we have inspected the sample under an optical microscope to see whether the pattern has been clear and well defined. If the results are not good, the hard bake should not be performed. If everything looks okay, the sample was placed onto the hard bake plate that was heated to 105 ^{0}C. The sample was remained on the plate for 5 minutes to prepare it for the etching process. This step is necessary in order to harden the photoresist and improve adhesion of the photoresist to the sample surface.

- For the etching, we used chemical (wet) etching process that utilizes liquid chemicals or etchants to remove regions of the underlying material that are no longer protected by photoresist after development. Wet etching is generally isotropic, i.e., it proceeds in all directions at the same rate. An etching process that proceeds in only one direction (e.g., vertical only) is said to be 'completely anisotropic'. Wet etching is not practical for use in pattern images that have features measuring less than 5 microns due to the fact that an isotropic etchant eats away a portion of the material under the mask. The bolometer patterns with features that are smaller than 5 microns must not be wet-etched, and should instead be subjected to other etching techniques that offer a higher degree of anisotropy. For chemical etching we used 0.2 ml 0.75% H_3PO_4 acid diluted with 40 ml DI water for duration of 30 to 60 seconds depending on thickness of the superconducting thin film. Then the device was washed with DI water and blow-dried until no droplet is left.

- The bolometer was then placed in acetone baths for 2 minutes to remove the photoresist from the unexposed area and then Isopropyl alcohol was used to ensure no residue from acetone remains.

Examples of bolometer patterns used in this study are illustrated in Figure 3.5. According to the pattern area and response behaviours, we have classified and named the devices used in this thesis as L_1, L_2, S_1, and S_2. L_1 and L_2 are large area bolometers that have line widths of 50 and 100 μm and effective areas of 1.7 and 6 mm^2 respectively. S_1 and S_2 are a small area spiral bolometer and a microbridge, which have line widths of 10 and 12 μm and effective areas of 0.012 and 0.003 mm^2 respectively.

3.1.4 Contact Metallization

For contact pads of the YBCO patterns, we deposited ~ 80 nm thick gold layer after pre-etching the YBCO for approximately 5 nm. For this purpose, we have used Denton Vacuum Desk II etch-sputter unit and copper shadow mask fabricated with standard Printed Circuit Board (PCB) printing process. For the wire contacts we used the thinnest copper wire possible to decrease the thermal conduction via the wires. Copper wired contacts were made using silver epoxy resulting in very low resistance (< 0.1 Ω) contacts at low temperatures.

3.2 Characterization Setup

The characterization setup shown in Figure 3.6 mainly consists of a liquid nitrogen based dewar, a computer controlled current source for biasing the bolometers, a power supply and digital multimeter for controlling the temperature of the system, a DSP lock-in amplifier for measuring the magnitude and phase infrared response, laser source of 850 nm wavelength, and data acquisition board for connecting all the units together and automating the operation of the system. The setup fulfils controlling temperature, making four-probe resistance versus temperature measurements, and measuring the phase and magnitude of the IR-response of the bolometer.
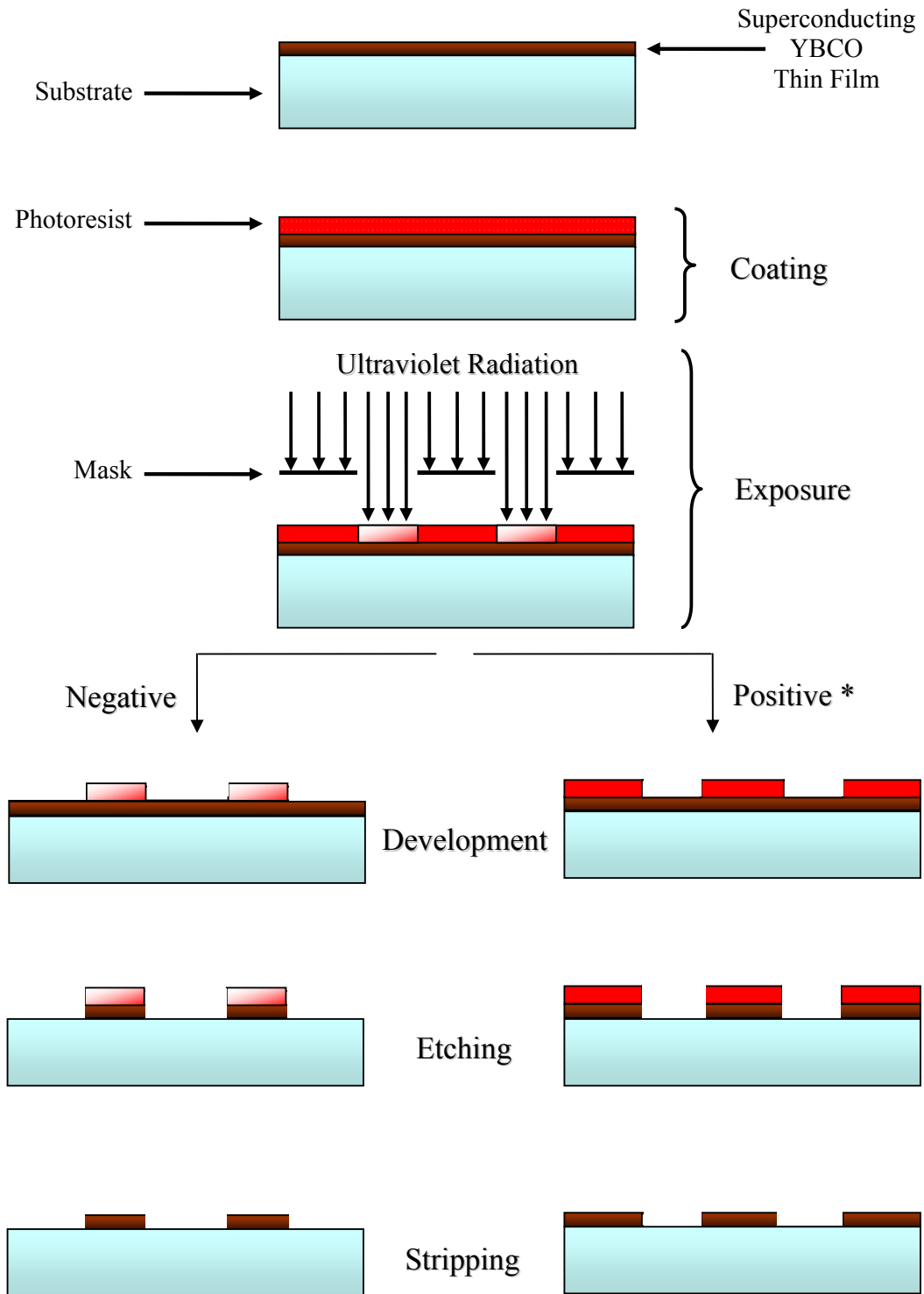
Figure 3.4: The photolithographic process and etching for fabrication of the bolometers. The superconducting thin film used in this study was coated with positive AZ5214 photoresist material. The physical dimensions are not to scale.
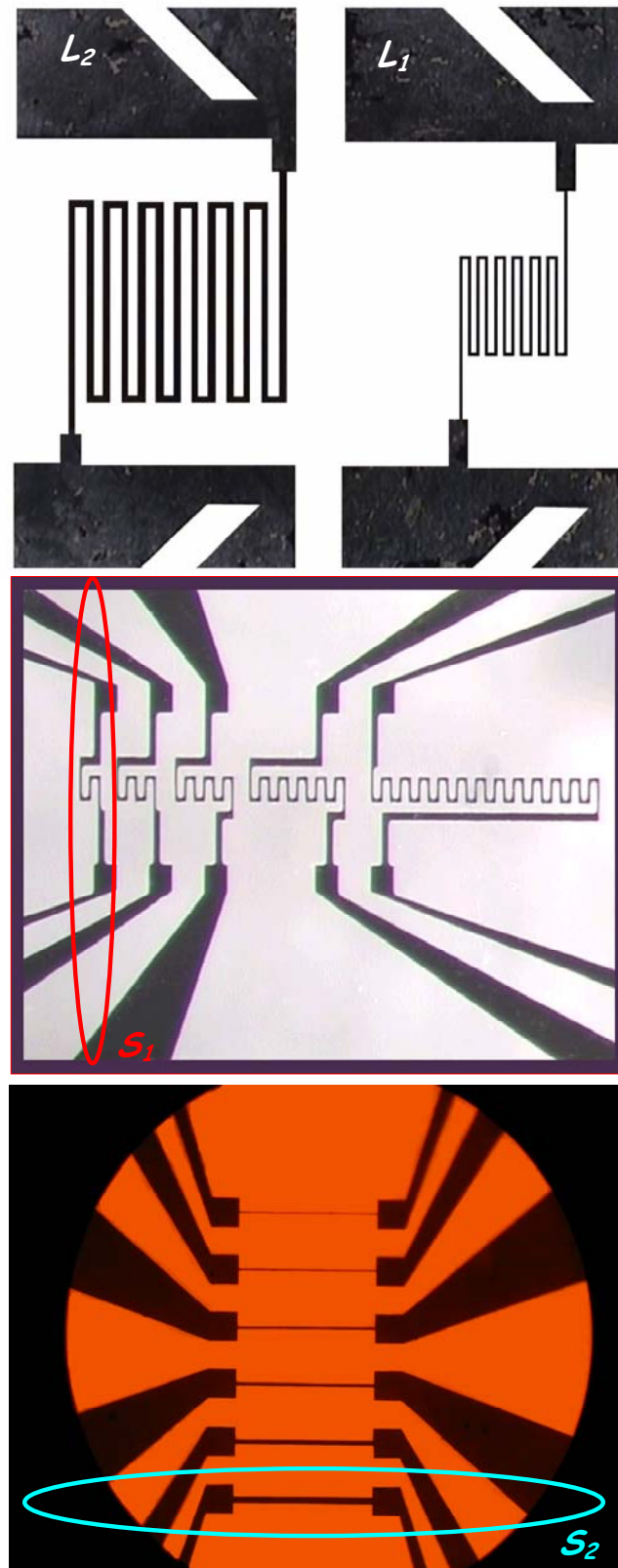
Figure 3.5: The patterns of the bolometers designed on the superconducting YBCO thin films.
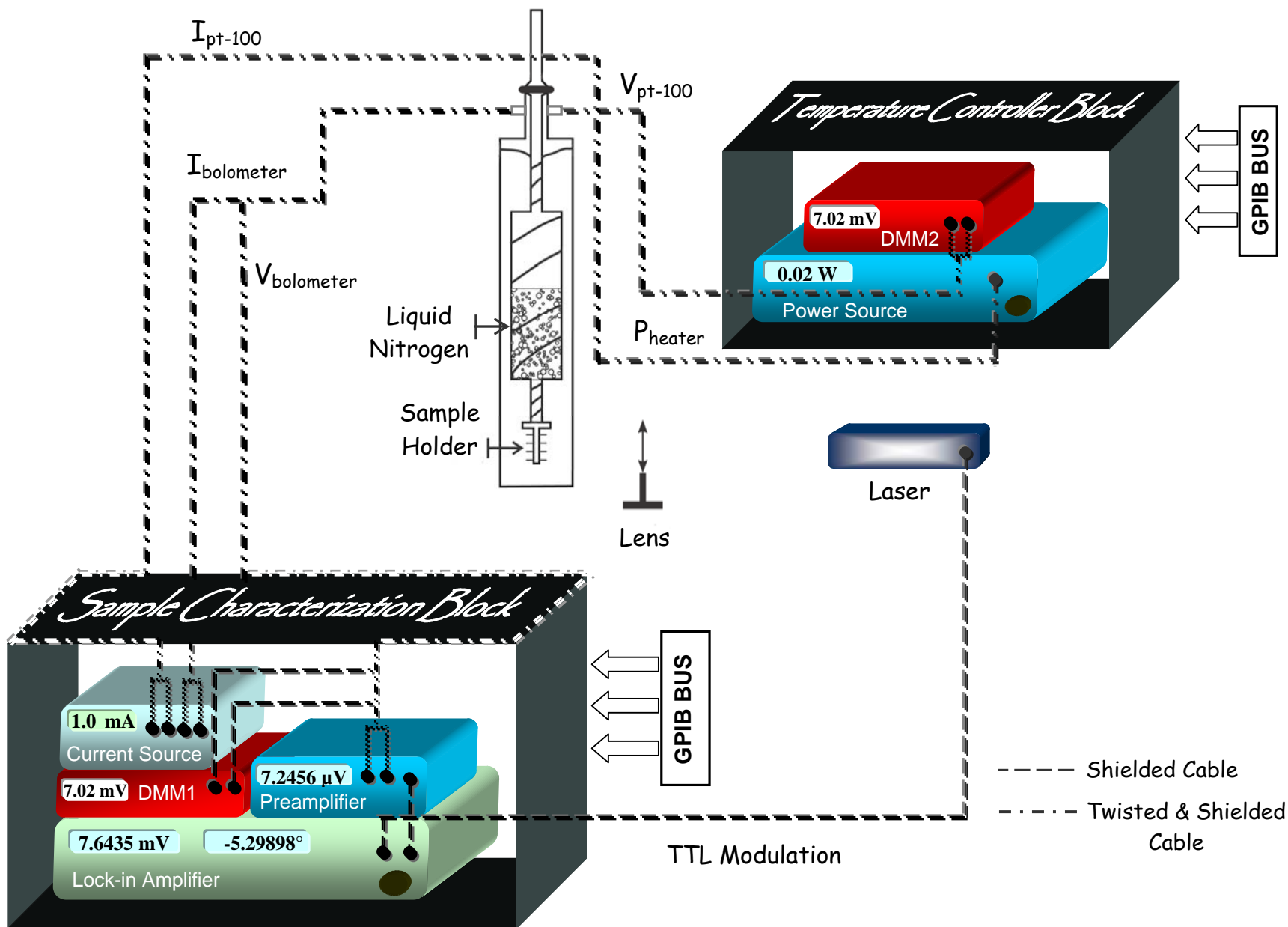
Figure 3.6: Block diagram of the characterization setup with electrically modulated infrared laser
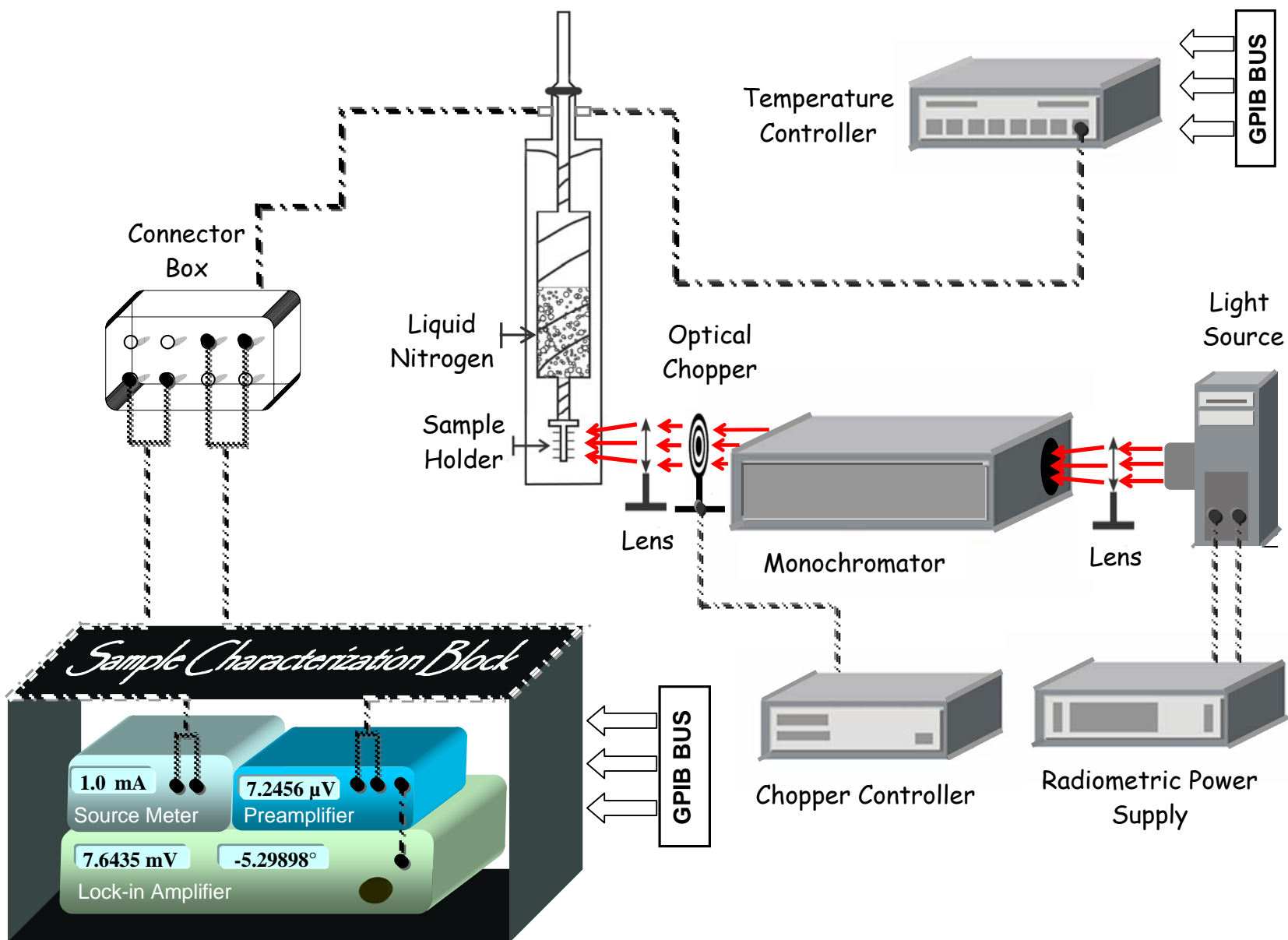
Figure 3.7: Block diagram of the characterization setup for wavelength dependence measurement

IR Radiation

YBCO Thin Film

Substrate

**Sample Holder
(Cold Head)**

Pt - 500 (Temperature Sensor)

Figure 3.8:   Configuration of the thin superconducting film samples on a crystalline substrate in contact with the holder and the temperature sensor.

To cool the samples, a liquid nitrogen based Dewar (Janis VPF-475) with a cold finger was used. The configuration of superconducting sample, sample holder, and temperature sensor is illustrated in Figure 3.8. The sample holder was designed and made of high purity and highly conductive oxygen-free copper. To improve the thermal contact between the substrate and c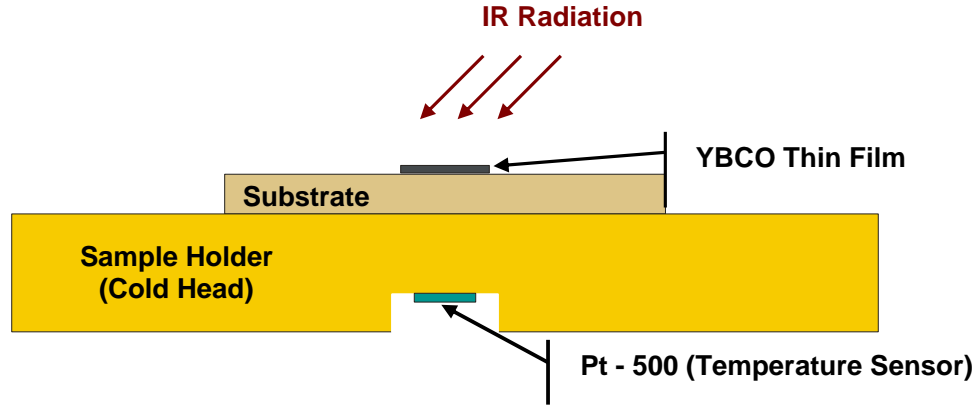old-head, a very thin layer of vacuum grease was applied to the back side of the substrate. Temperature of the devices was controlled with PID controller software within maximum 20 mK deviation from the target temperature. Pt-500 was used as a temperature sensor which has a linear temperature dependent resistance in liquid nitrogen-room temperature range. The sensor was calibrated by measuring the resistance in LN (77.3 K) and ice water (273.7 K), and finding the linear relation between temperature and the resistance. The resistance of Pt-500 was measured with 4-wire resistance measurement method using Agilent 3401A Digital Multimeter (DMM2) with 100 μA bias current to prevent self-heating. The sensor was mounted in a groove, 1 mm below the sample so that the temperature gradient was minimized. The metal film resistor heater powered by an HP6628A DC power supply was placed 1 cm away from the sample and can control the temperature up to 150 K with a maximum power of 5 W. For the temperatures close to 90 K, 1-2 W is sufficient and 250 ml of Liquid Nitrogen provides cooling the Dewar for 2 hours. The thermal conductance from the cold head to the LN reservoir was intentionally decreased by adding some insulator in between so that the thermal run away from the cold head is further decreased. The temperature controller can increase or decrease the temperature of the system by up to 5 K/min. For the temperature sweep measurements, 1 K min^{-1} heating and cooling rate

was used to minimize temperature gradient between the sample and the temperature sensor during the measurement. In this case we obtained a deviation of 10 mK.

The bolometers were radiated by an electrically modulated laser source of 850 nm wavelength with a power output of 12 mW. Because of quartz windows of the liquid nitrogen based Dewar not being close enough to the sample, a lens was used to focus the light to get higher intensity without losing the homogeneity of the light on the patterns.

The responses of the samples were measured by applying a stabilized DC bias current (I_{bias}) in four probe configuration using an automated low noise characterization setup. The measurement of the phase and magnitude of the photoresponse was done by using a SR 850 DSP lock-in amplifier, the input of which was amplified with a SR 570 ultra low noise preamplifier.

In this study, we performed three major measurements on the small and large area bolometers patterned on MgO substrates to investigate the temperature and modulation frequency dependence of the thermal parameters, and the effect of the superconducting transition width on the infrared response of the bolometers by using the characterization setup. The measurements are; resistance versus temperature, the phase and magnitude of the response versus the temperature at fixed frequency and versus modulation frequency at fixed temperature. During the measurement of the resistance with respect to temperature, we biased the bolometers with an appropriate current and decreased the temperature at which resistance of the bolometer becomes zero, $T_{c\text{-zero}}$. Then we increase the temperature with 1 K/min heating rate from $T_{c\text{-zero}}$ to normal state temperature and record the voltage across the bolometers. This measurement is required to investigate the DC characteristics, joule heating effect, and thermal stability of the bolometers. In the response versus temperature measurements, we measured the phase and magnitude of the response of the bolometer while sweeping the temperature of the sample between zero resistance temperature $T_{c\text{-zero}}$ to onset temperature $T_{c\text{-onset}}$ at fixed modulation frequencies 1 Hz, 11 Hz, 110 Hz, 1100 Hz, and 11 kHz. In the measurement of the response with respect to modulation frequency, while recording the phase and magnitude of the response of the bolometer, we swept the modulation frequency between 0.1 Hz to 100 kHz and kept the temperature of the sample at $T_{c\text{-zero}}$, T_c, and $T_{c\text{-onset}}$.

The physical properties of the measured devices such as pattern areas, pattern types, the thicknesses of MgO substrates, critical temperatures (T_c), the slopes of

resistance versus temperature curve at critical temperatures (dR/dT), and the transition widths (ΔT) are summarized in Table 3.1

Table 3.1: The physical properties of the measured devices fabricated on MgO substrate

Device Code	Pattern Area (mm^2)	Pattern Type	MgO Substrate Thickness (mm)	T_c (K)	ΔT (K)	dR / dT (Ω /K)
L_1	1.7	Meander (large)	1	88.5	1.4	1829
L_2	6	Meander (large)	1	87.2	2.6	1989
S_1	0.012	Meander (small)	1	90.3	3.2	493
S_2	0.003	Microbridge	0.5	89.2	6	629

The characterization setup for the wavelength dependence of the optical response measurement shown in Figure 3.7 consists of a Janis VPF-100 liquid nitrogen based dewar to cool the samples, a Keithley 2400 sourcemeter to bias the devices, a SR-830 DSP lock-in amplifier for measuring the optical response, a SR-570 low noise preamplifier and a Lakeshore 331 temperature controller. The sample was illuminated by an Oriel spectral light source with condenser. This instrument used a 100 W quartz tungsten halogen lamp to produce a beam with wavelengths over the spectral range of 0.2-2.7 μm. It was operated with a radiometric power supply with its operating current and the voltage values adjusted to 8.34 A and 12 V. We used a grating monochromator (Oriel-77200) to obtain a selected single spectral line from a broadband (multi-wavelength) light source in order to investigate the effect of incident wavelength on the response of devices. Spectral range of the monochromator, from 200 nm to 24 μm, corresponds roughly to photon energies from 6.2 eV to 52 meV. The beam was collimated with two convex lenses of 127 mm and 48 mm focal lengths. It was then passed through an optical chopper wheel and entered the sample chamber through a quartz window. All optical elements, as well as the sample chamber itself, were mounted on a standard optical bench for ease of positioning.

In this work, we performed the measurements on the large area bolometers L_1 and L_2 patterned on MgO substrates to investigate the wavelength dependence of the optical response of the bolometers. We measure the magnitude of the optical response as a function of the incident wavelength from 400 nm to 730 nm at bias current of 1 mA and modulation frequency of 11 Hz. The measurements for devices L_1 and L_2 were performed at temperatures 88.5 K and 87.2 K respectively.

The power of the incident beam produced by quartz tungsten halogen lamp was varying rapidly with wavelength. In order to characterize the bolometric photoresponse of the devices, the actual power density at the sample, not just a relative density, had to be found. Therefore, the magnitude of the response has been calibrated with data measured from powermeter mounted in front of the cryostat. The results and their analysis will be discussed in more details in the next chapter.

CHAPTER 4

EXPERIMENTAL RESULTS AND DISCUSSION

4.1 Structural Characterization of YBCO Thin Films

The $YBa_2Cu_3O_{7-\delta}$ thin films of 200 nm thickness were grown on single crystal (10 x10 x 0.5-1 mm^3)-sized MgO (100) substrates by DC inverted cylindrical magnetron sputtering. The thin films were characterized by structural, morphological, compositional and electrical analyses. Structural analysis is performed by means of X-Ray Diffraction (XRD) from which we can obtain information on the phases and their crystallographic orientation with respect to the substrate. The Scanning Electron Microscope (SEM) and Atomic Force Microscopy (AFM) give information on the film morphology and the Energy Dispersive X-ray analysis (EDX) distinguishes the chemical species analyzing the x-rays emitted from the samples when they are hit by the SEM electron beam.

XRD patterns of the YBCO thin film grown at optimized growth parameters are shown in Figure 4.1. The full width at half maximum (FWHM) value of (005) diffraction peak of samples is employed to represent the thin film crystalline quality. The FWHM value of the rocking curve of the (005) peak characterized the degree of alignment of the c-axis with the normal to the substrate (Liu et al. 2002). In literature, the FWHM value of about 0.48º has been reported (Tsukamoto et al. 2003). In our study, the FWHM value measured from rocking curve of the YBCO (005) peak was about 0.268º, indicating a highly *c*-axis oriented thin film.

Energy depressive x-ray spectroscopy, EDX or EDS, is a chemical microanalysis technique performed in conjunction with a scanning electron microscope SEM. In this technique, an electron beam of 10-20 keV strikes the surface of a conducting sample which causes X-rays to be emitted from the point of incidence. The x-ray detector measures the number of emitted x-rays with respect to their energy. By collecting and analyzing the energy of these X-rays, the constituent elements of the specimen can be determined. EDX analysis results of the YBCO thin film are given in Figure 4.2. From the EDX spectrum we identified the elements Y, Ba, Cu, O, and Mg present in the YBCO sample. From this analysis, we found that there is no detectable impurity phase in the YBCO structure.
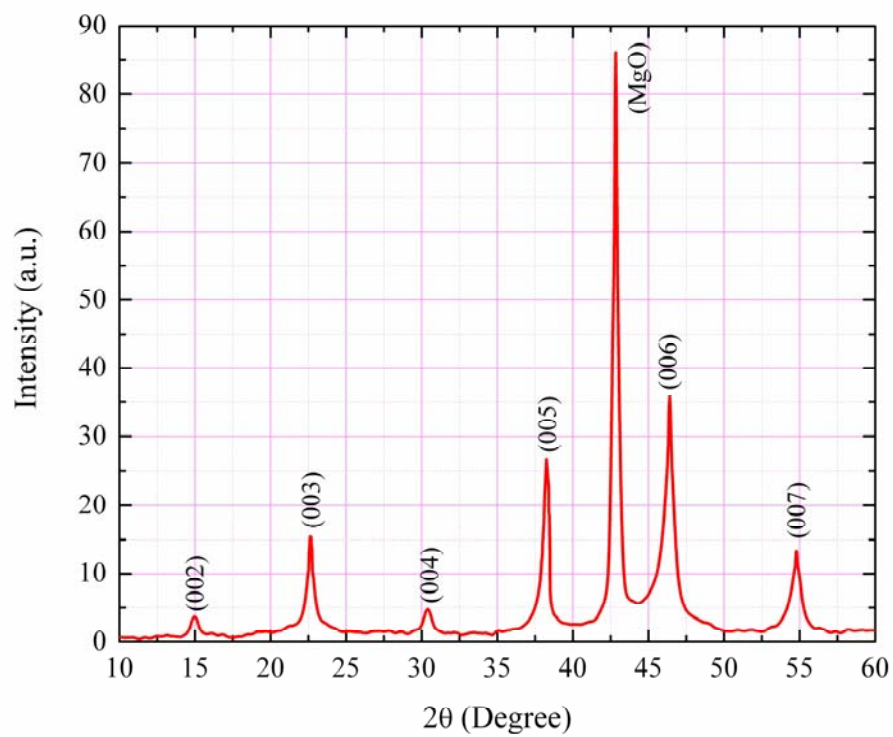
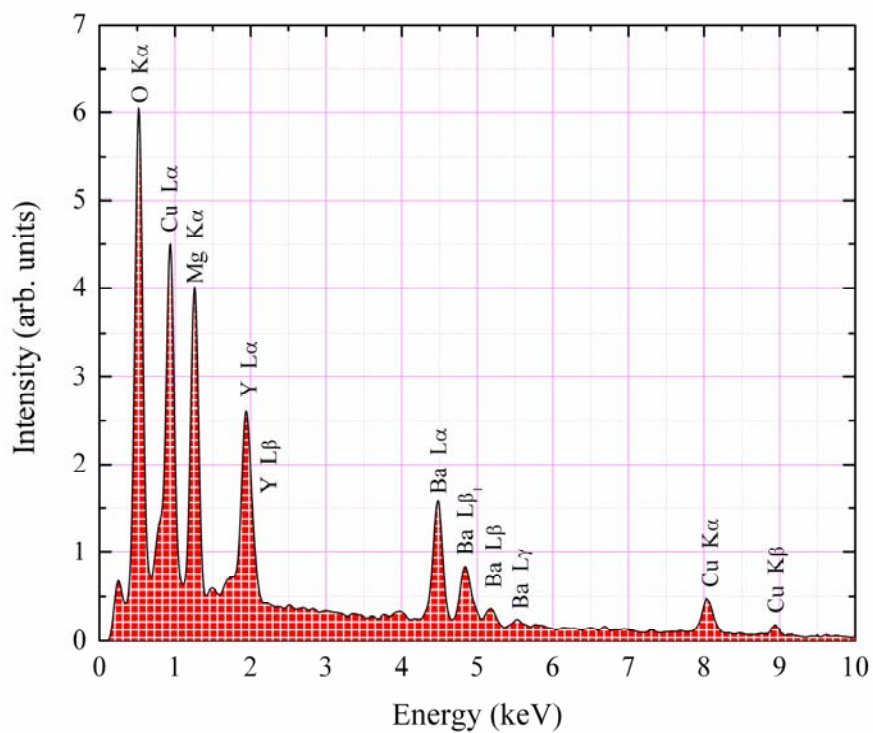Figure 4.1: XRD patterns for YBCO thin film grown on MgO substrate

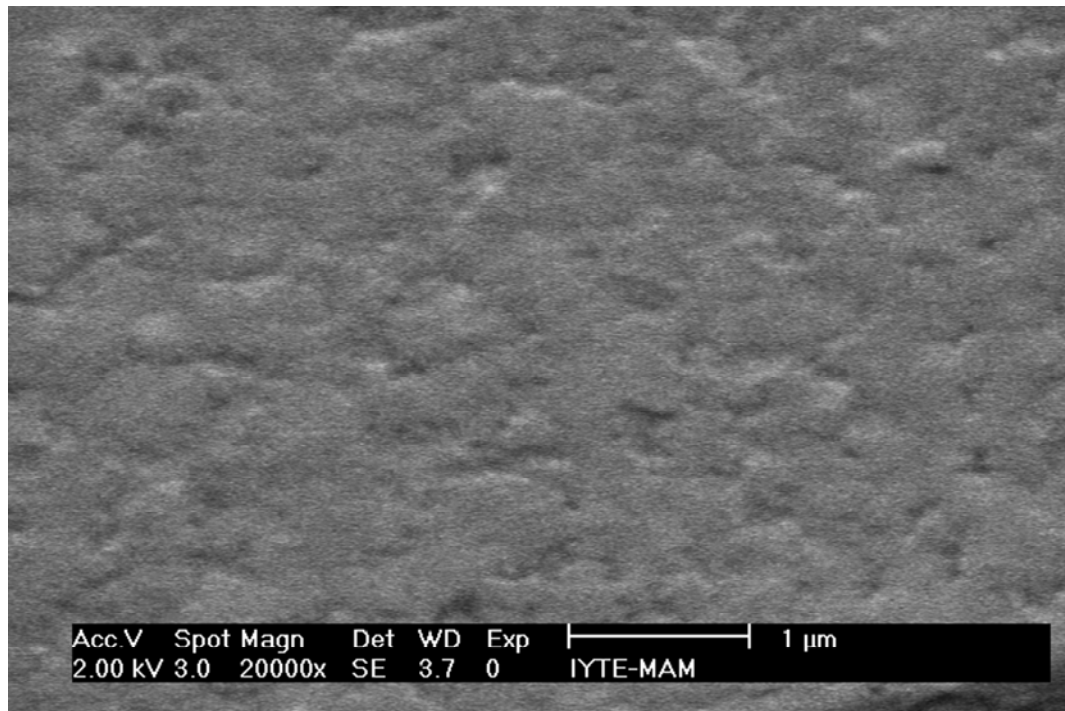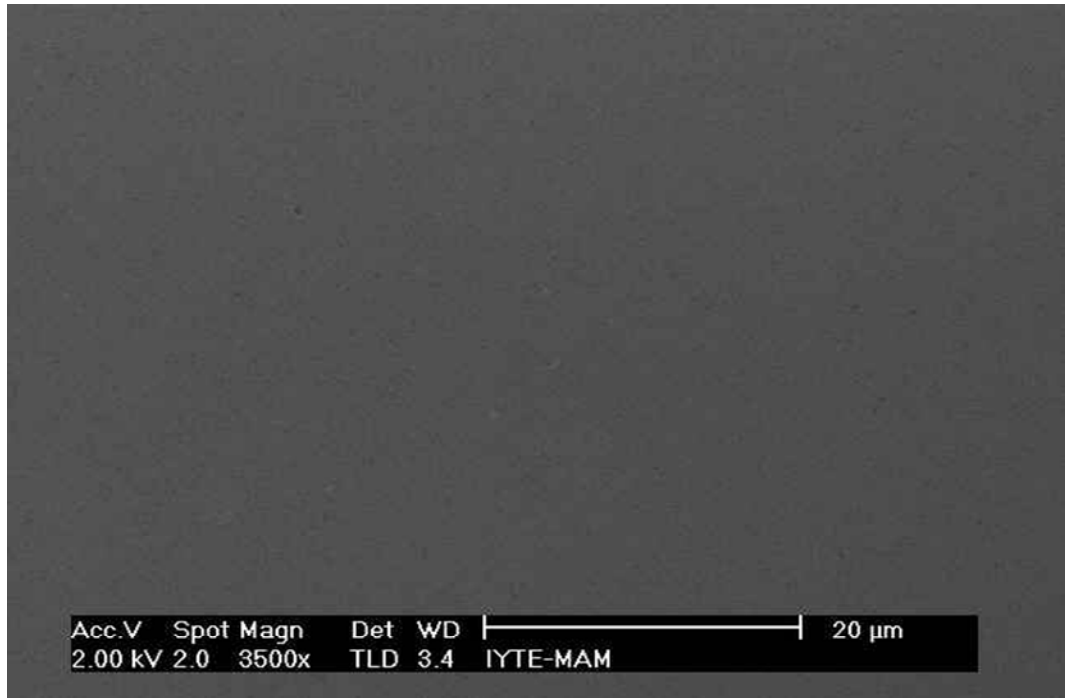Figure 4.2: EDX analysis for the YBCO/MgO sample

Figure 4.3: SEM micrographs of the YBCO thin film deposited on MgO substrate at (a) 3,500x and (b) 20,000x magnifications.

The microstructures of the films were also studied by SEM. This is essential in order to get a comprehensive picture of the assemblage of crystallites and the continuity of the film. The SEM employs a focused beam of electrons, with energies typically in the range from a few hundred eV to about 30 keV, which is rastered across the surface of a sample in a rectangular scan pattern. Secondary electrons (SE) with low energy are ejected from the outer shell of sample atoms after inelastic interaction with incident electrons. Then, they are collected by a positively charged detector which is scanned in synchrony with the emission beam scan. SEM micrographs of the YBCO thin film are shown in Figure 4.3.a, b. They were taken at 3500x and 20,000x magnifications with 20μm and 1μm resolutions at operating voltage of 2 kV respectively. They show that the film has a high density as well as crack-free and flat surface. The morphology of the film was found to be uniform throughout the surface. The absence of pores proves good growth of the YBCO thin film on the MgO substrate. The AFM image was also taken to provide a clear insight into the surface morphology of the YBCO sample. The surface of the film was found to be quite smooth as illustrated in Figure 4.4. The mean surface roughness, R_a, of the YBCO thin film grown on MgO substrate within scanned area of 5 x 5 μm^2 was measured as about 5.679 nm. This value is in well agreement with the SEM results about the smoothness of the samples.
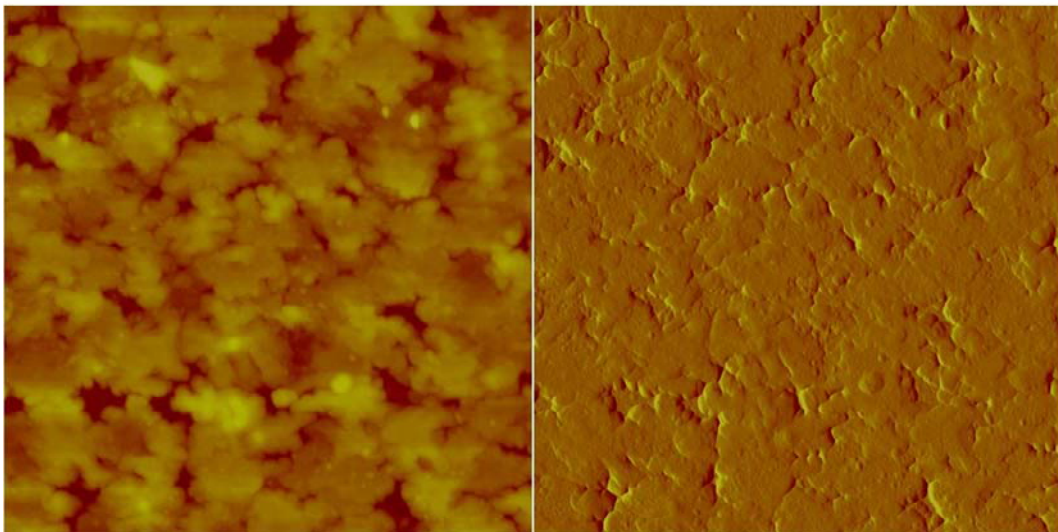

Figure 4.4: AFM surface roughness analysis of the YBCO thin film within scanned area of $5\ x\ 5\ \mu m^2$

4.2 Electrical and Magnetic Characterization of YBCO Thin Films

To investigate the superconducting properties of the sputtered YBCO thin film, electrical and magnetic measurements were carried out by resistance versus temperature (R-T) and AC magnetic susceptibility, respectively. The sample has shown very sharp transition at temperature about 90 K as shown in Figure 4.5. Above the onset temperature of the superconducting transition, $T_{c\text{-}onset}$, the sample shows linear resistive behavior just like metals as shown in Figure 4.5. The normal state resistance value of the sample was measured about 28 Ω at 300 K.
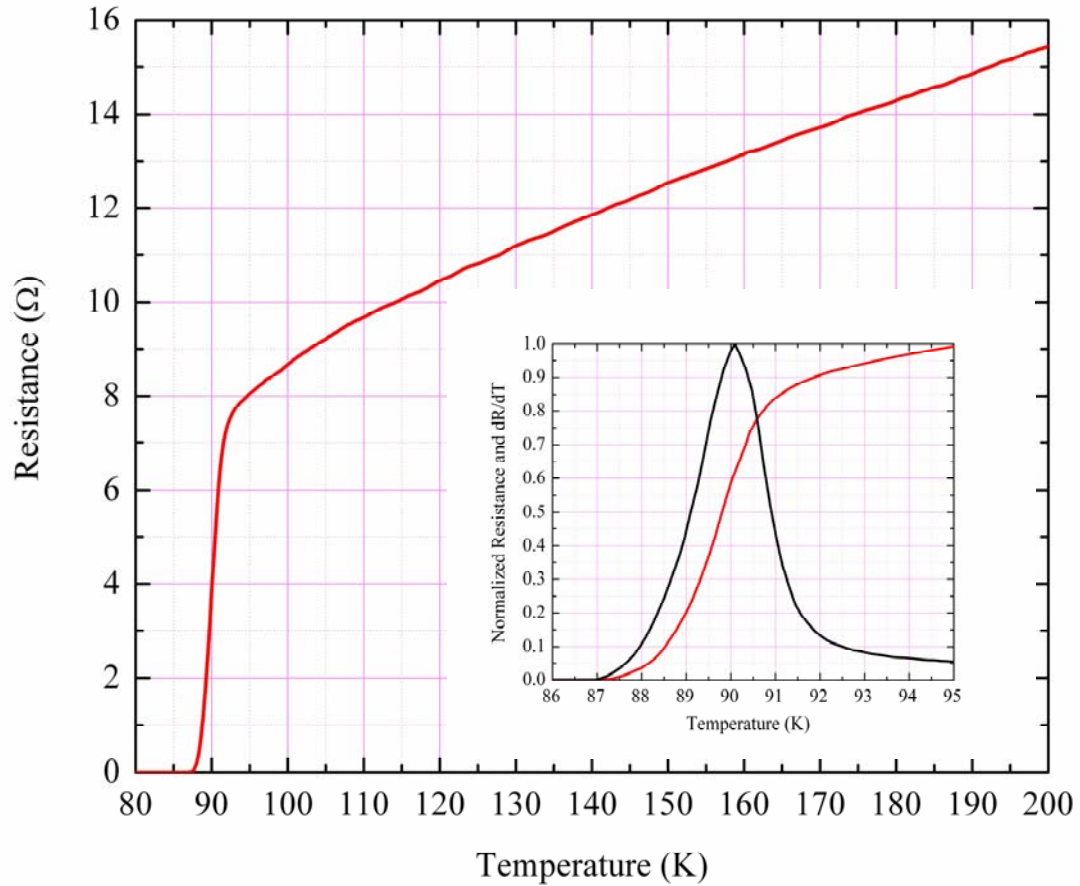

Figure 4.5:   Resistance versus temperature measurement for YBCO thin film. Inset shows normalized resistance and dR/dT curves at 86-95 K
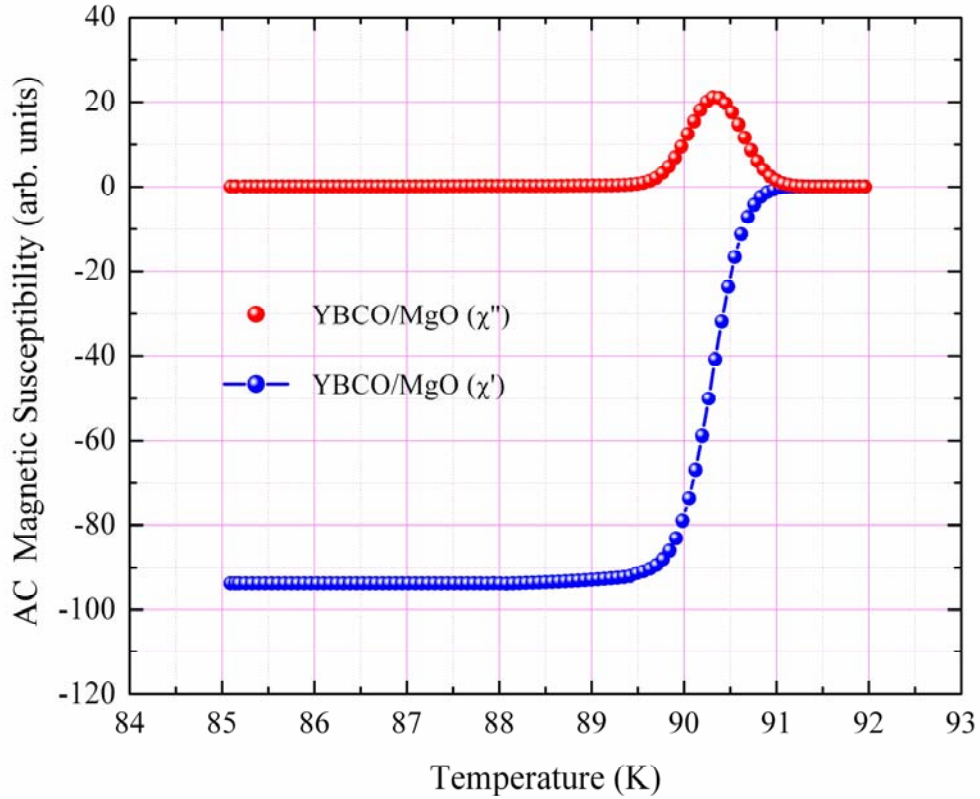
Figure 4.6:   Temperature dependence of real (χ') and imaginary (χ'') parts of AC
magnetic susceptibility for YBCO thin film

The AC complex susceptibilities (χ'-$i\chi''$) of the samples were measured in a two-coil system using a two-phase Lock-in amplifier to pick up in-phase (χ') and out-of-phase (χ'') signal of the secondary coil with AC magnetic field aligned perpendicular to the film surface. The excitation field within the primary coil was $h(t) = h_0 \sin 2\pi ft$ with $f = 1$ kHz and the amplitude h_0 was 18.5 A/m. The real (χ') and imaginary (χ'') parts of the AC magnetic susceptibility response for an applied magnetic field are depicted in Figure 4.6. The real part of susceptibility, χ', was observed to be stepwise as a function of temperature, representing transition from near-perfect screening to complete penetration of external AC magnetic field into the sample while the peak was observed in the imaginary part of susceptibility, χ'', being a measure of dissipation in the sample as shown in Figure 4.6.   Moreover, the sharpness of the transitions seen in Figures 4.5 and 4.6 indicates to the homogeneity and the strong diamagnetic property of the film. Thin films with lower quality have also been prepared by varying some of the

parameters for the purpose of determining the effects of film quality on the phase and magnitude of the response of YBCO edge transition bolometers to the near infrared radiation. The observations will be discussed in more detail in the section 4.4

4.3 Infrared Response Analysis of YBCO Edge Transition Bolometers

Dependence of the magnitude and phase of the infrared response of the devices on temperature and modulation frequency was investigated at a bias current of 1 mA. The infrared response versus temperature measurement on the small area bolometer S_1 is shown in Figure 4.7. As shown in the figure, the results of the IR-response versus temperature measurement are superimposed on its resistance versus temperature transition curve. There is a peak in the response at critical temperature of the sample that is due to the sharper transition of resistance with respect to temperature giving a higher dR/dT.

From Figure 4.8, we observed that the normalized magnitude of the infrared response of the devices is proportional to the slope of the resistance versus temperature curve, dR/dT. The strong match of the curves confirms the bolometric behavior, as described by equation 2.5. From the infrared response versus modulation frequency measurement, it can be observed that the infrared response at T_c for all modulation frequencies is higher than the response at $T_{c\text{-}onset}$ and $T_{c\text{-}zero}$ due to higher value of the temperature derivative of the resistance, dR/dT, at T_c. Moreover, the decrease in the infrared response due to increase in the modulation frequency for a small area device can be explained by reduction in thermal diffusion length which in other words causes a decrease in thermal resistance of the bolometer, shown in Figure 4.9.

We observed that the phase of the infrared response strongly depends on temperature at higher modulation frequencies as shown in Figures 4.8 and 4.9. The phase lag of the response at higher modulation frequencies, in the range of about 10-100 kHz, increased with increasing temperature as illustrated in Figure 4.9. Increase of the phase by lowering temperature in the high frequency range suggests a decrease in the film or substrate capacitance and an increase in the thermal conductance (Robbes et al. 1999).

The large area bolometer L_1 also showed similar infrared response behaviours with respect to temperature and modulation frequency as seen in Figures 4.10 a, b. However, in general, small area bolometers have less phase lag than the large area bolometers due to their relatively lower total thermal capacitance, that is; the formers are faster than the latters.

As a final all above mentioned results depict that the behavior of phase and magnitude of the infrared response with respect to temperature and modulation frequency can be interpreted to be due to the change of the thermal conductance and thermal capacitance of the bolometers for a fixed bias current and absorbtivity.
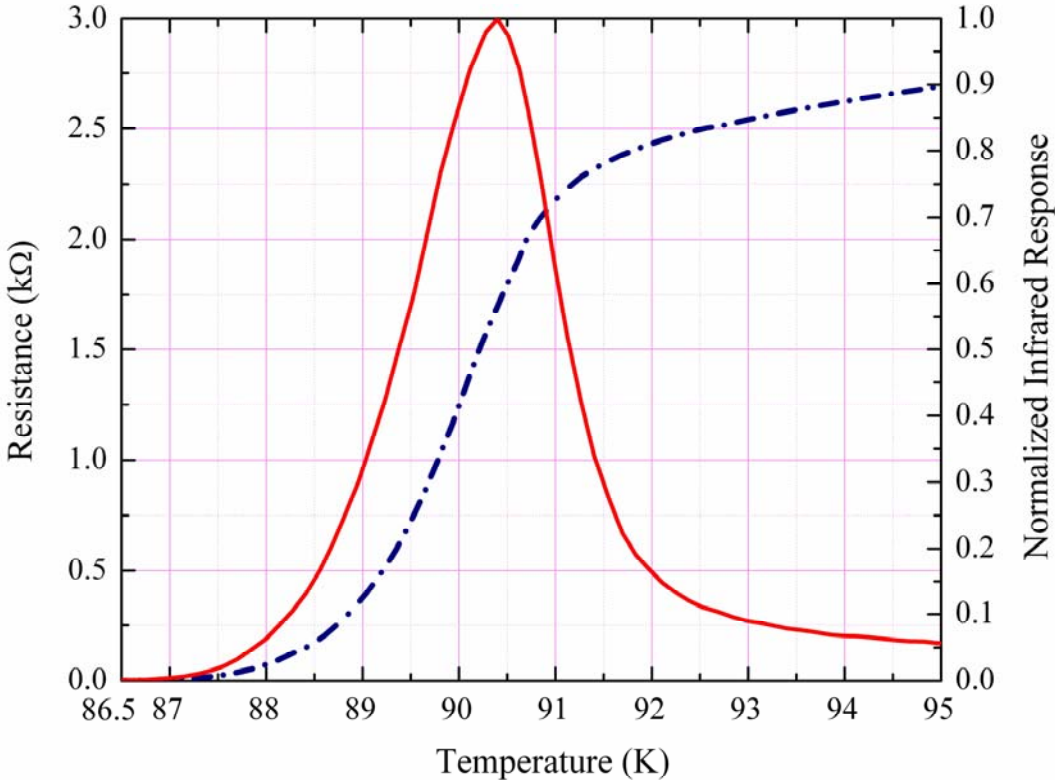
Figure 4.7: Temperature dependence of resistance and normalized infrared response for the small area bolometer S_1.
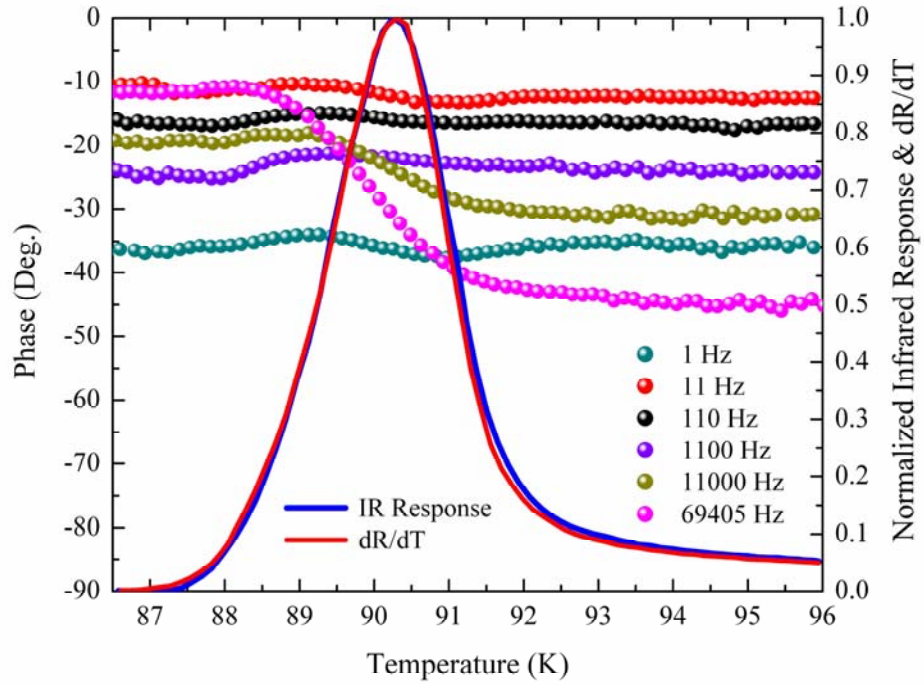
Figure 4.8: The magnitude & phase of the IR response and dR/dT of the small area bolometer S_1 as a function of temperature at various modulation

Figure 4.9: The magnitude and phase of the IR response of the bolometer S_1 as a function of the modulation frequency at $T_{c\text{-}onset}$, T_c, and $T_{c\text{-}zero}$.

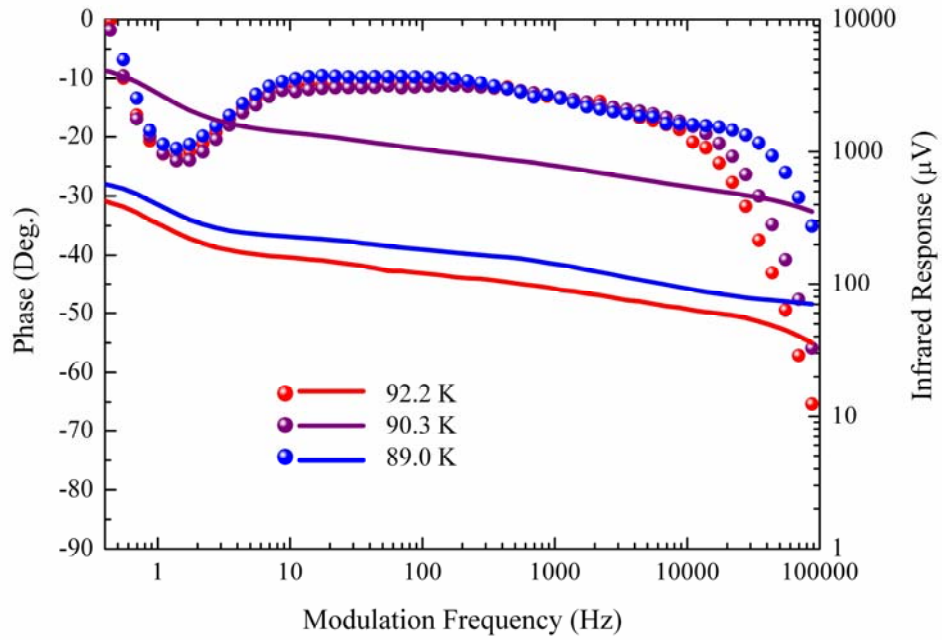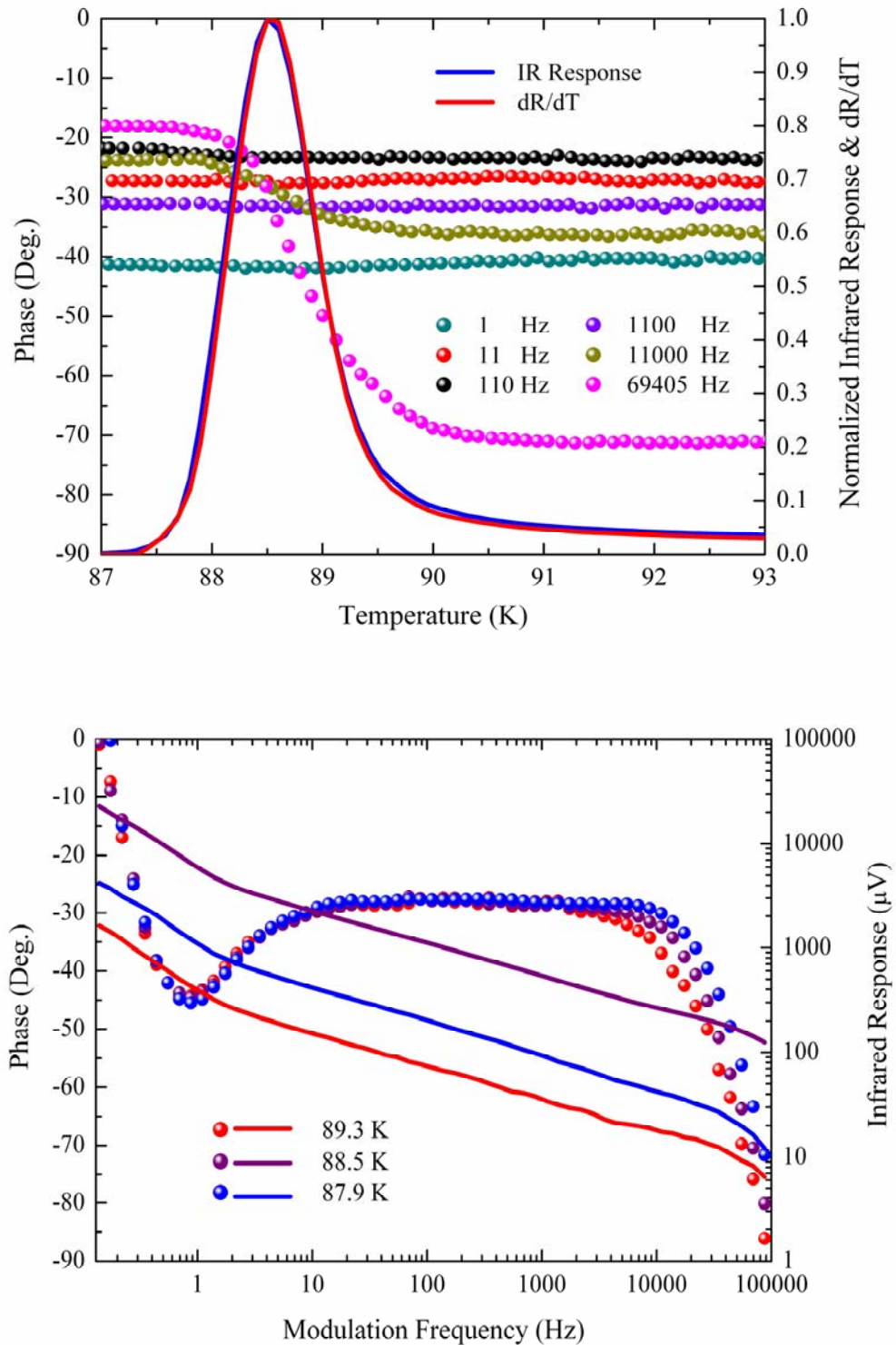Figure 4.10: The magnitude & phase of the IR response and dR/dT of the large area bolometer L_1 (a) as a function of temperature at various modulation frequencies ranging from 1 Hz to 69405 Hz and (b) as a function of the modulation frequency at $T_{c\text{-}onset}$, T_c, and $T_{c\text{-}zero}$.

4.4 Dependence of the Response on the Superconducting Transition Width of MgO Substrate YBCO Edge Transition Bolometers
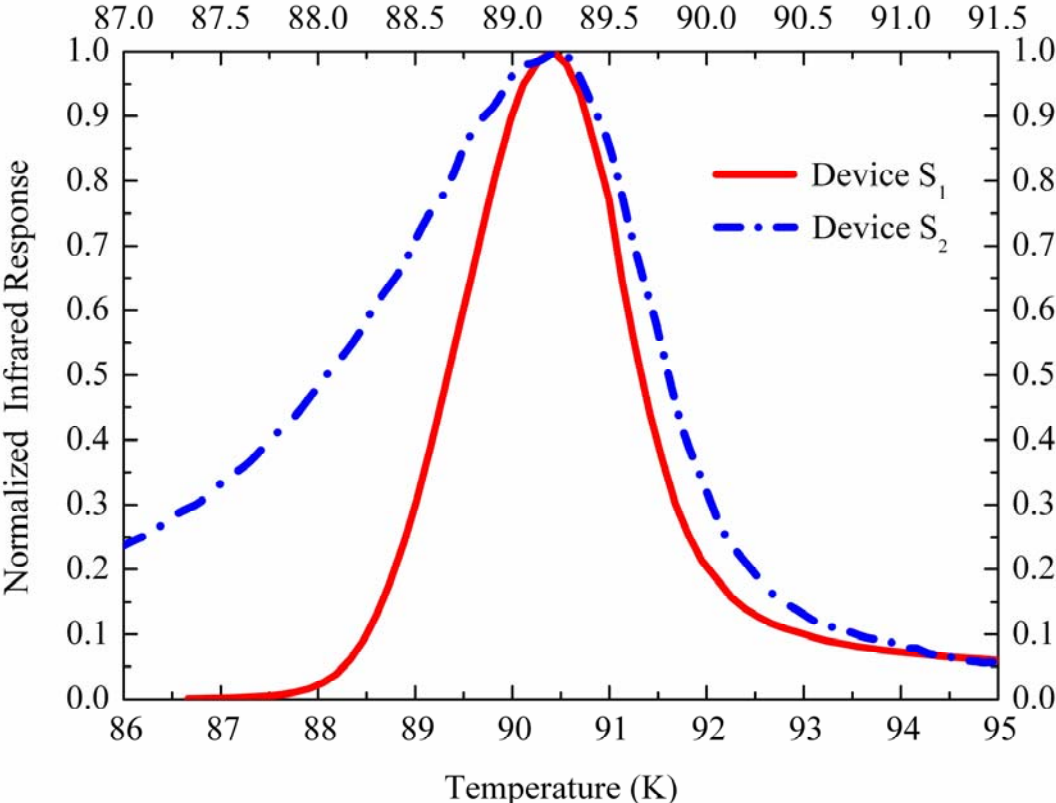

Figure 4.11: The normalized magnitude of the IR response of the small area bolometers S_1 and S_2 versus temperature measured at 110 Hz, f_m. Upper and bottom scales represent the temperature of the devices S_2 and S_1 respectively.

The fabricated YBCO bolometers resulted in different transition widths ΔT, as shown in Figure 4.11. The corresponding superconductive transition widths of S_1 and S_2 devices are 3 K and 6 K, respectively. The dependence of the transition width on oxygen content has been studied by some groups. For example, Ye et al. (1993) and Cogollo et al. (2003) ascribe the broad resistive transitions of the YBCO bolometers to the amount of oxygen deficiency and Uchiyama et al. (2004) attribute it to the nonuniformity of the oxygen content (7-δ) in the YBCO thin film. We investigated the effect of precipitates on the superconducting transition width. These observed precipitates might be outgrowth of Cu-rich oxide and inclusion of Y_2O_3 on the surface

of the YBCO thin films (Selinder et al. 1992, Lu et al. 1992, Han et al. 1994). The samples with high concentration of precipitates shown in Figure 4.12a are found to have broad superconducting transition width whereas the samples without precipitates seen in Figure 4.12b are found to have narrow transition width. Thus, by this observation, we conclude that the concentration of the precipitates in our films has direct influence on the transition width of the bolometers.

In this work, we studied the dependence of the response characteristics of the devices on the superconducting transition width of the samples on MgO substrates. We have investigated the observed features on the magnitude and the phase of the response with respect to f_m, such as a dip in the phase of the response versus f_m curve around 1 Hz, the amount of variation in the magnitude of the response, and dependence of the phase of the response on the temperature at mid-range modulation frequencies.

As shown in Figures 4.13 and 4.14, the devices with large transition widths showed a phase dip around $f_m = 1$ Hz that degraded the magnitude of the response even at higher modulation frequencies. However, the phase dip of the response curve of the films with narrow transition widths was less, resulting in an increase in performance in the response magnitude and speed of the bolometers in the whole measured range of the modulation frequencies. Similar response characteristics have been observed before, however the responsible mechanisms were not investigated specifically (Fardmanesh 2001). The decrease of the phase and relative decrease of the magnitude of the response of the samples with wider transition suggest an overall higher thermal capacitance compared to that of similar devices with narrower transition width. This might be interpreted to be due to the difference in the characteristics of the generated phonon spectra of the YBCO film depending on their transition width.

The phase of the response of the films with narrow transition did not show considerable temperature dependence at mid-range modulation frequencies. However, the phase of the films with wide transition, showed considerable temperature dependence as shown in Figure 4.15.

Using Figure 4.16, we can observe the correlations between superconducting transition width, which is affected by the surface morphology of the film, and the resistivity of the YBCO bolometers. The resistivity of the small area bolometer S_2, having broad superconducting transition, is higher than that of the bolometer S_1, having narrow transition. The large area bolometers L_1 and L_2 also showed similar resistivity behaviours.
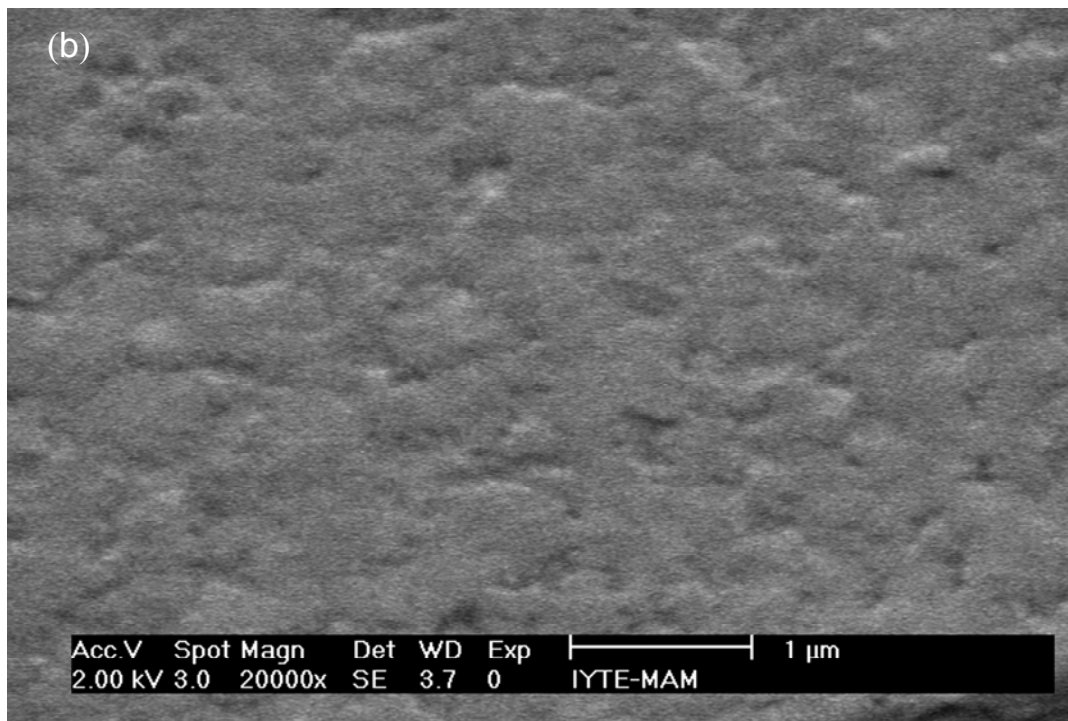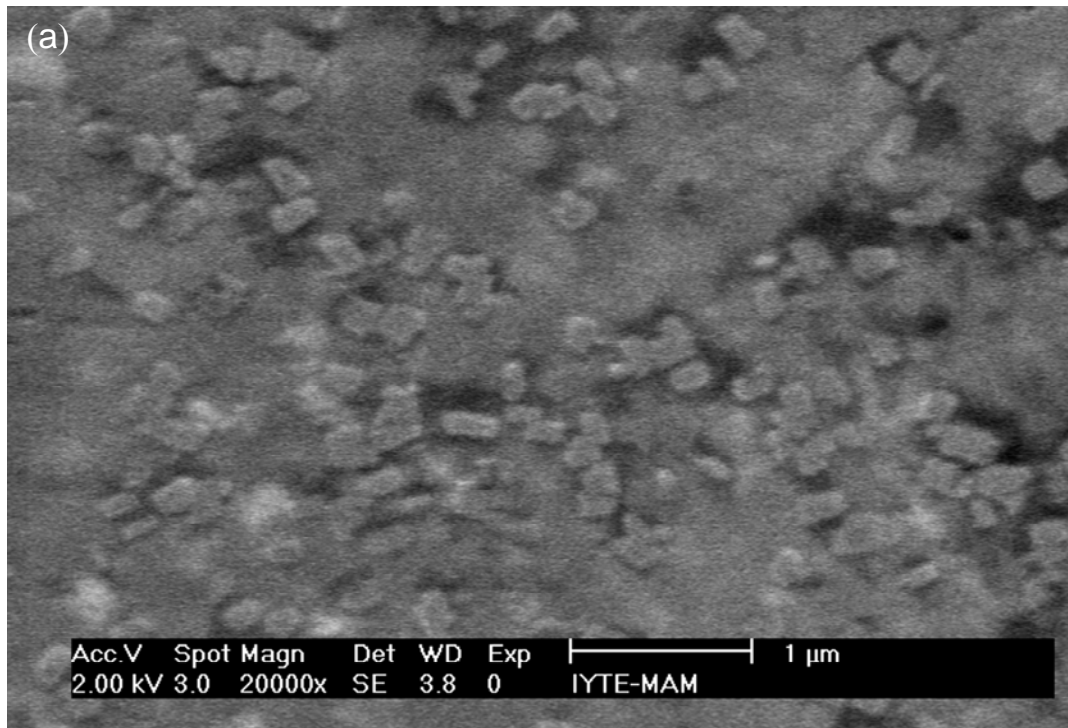
Figure 4.12:   Surface morphology SEM micrographs of the devices (a) with wide
transition width and (b) with narrow transition width

Figure 4.13: The phase and magnitude of the IR response of the small area bolometers S_1 and S_2 versus f_m measured at temperatures around T_c.

Figure 4.14: The phase and magnitude of the IR response of the small area bolometers
. L_1 and L_2 versus f_m measured at temperatures around T_c.
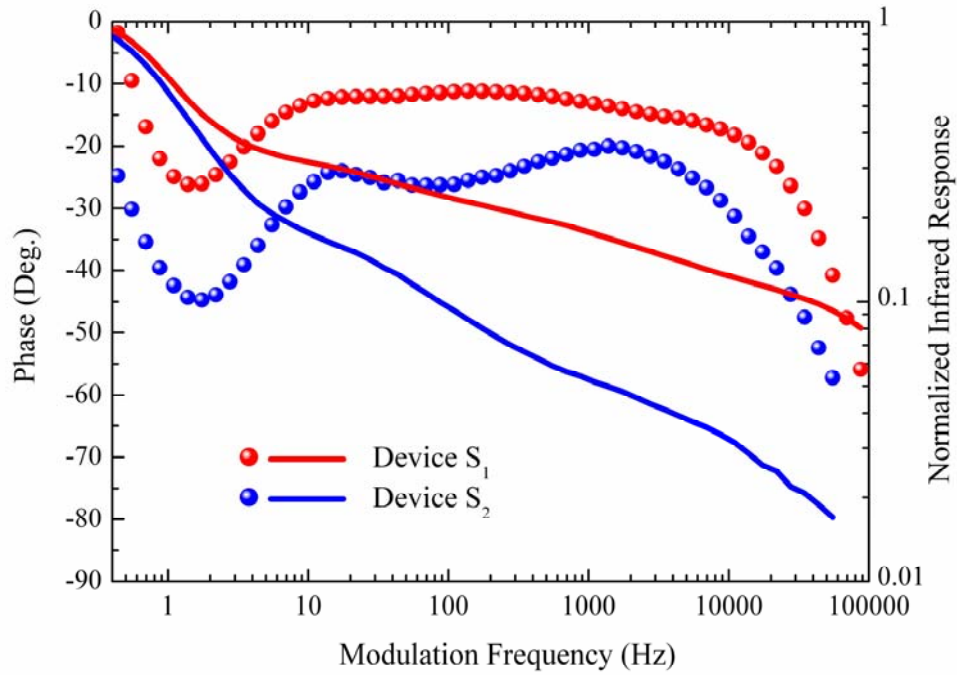
Figure 4.15: The phase of the IR response of the small area bolometers S_1 and S_2 versus f_m measured at temperatures around $T_{c\text{-}zero}$ and $T_{c\text{-}onset}$.
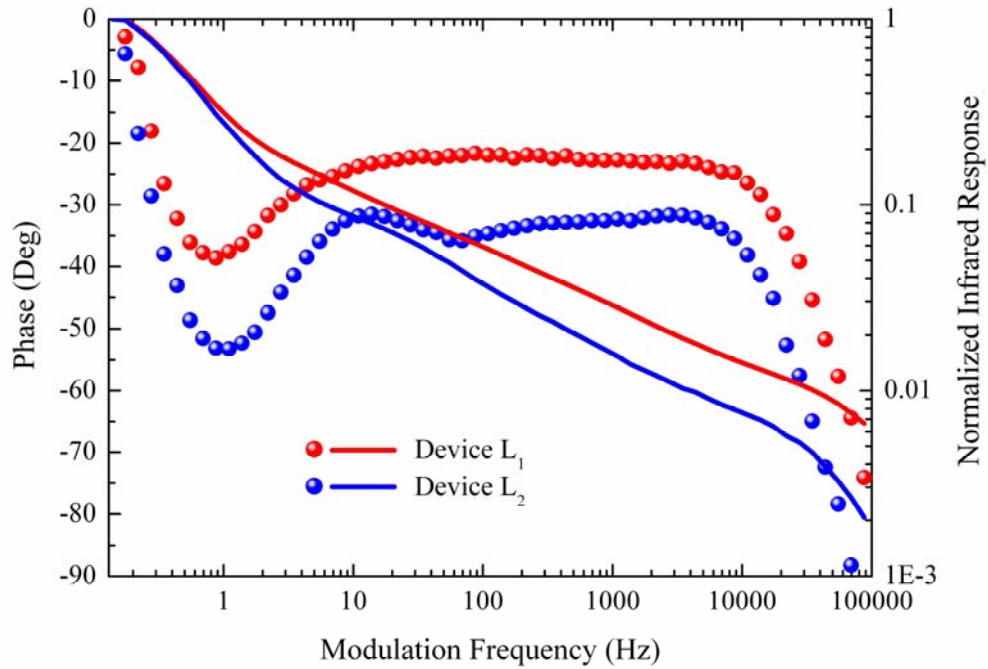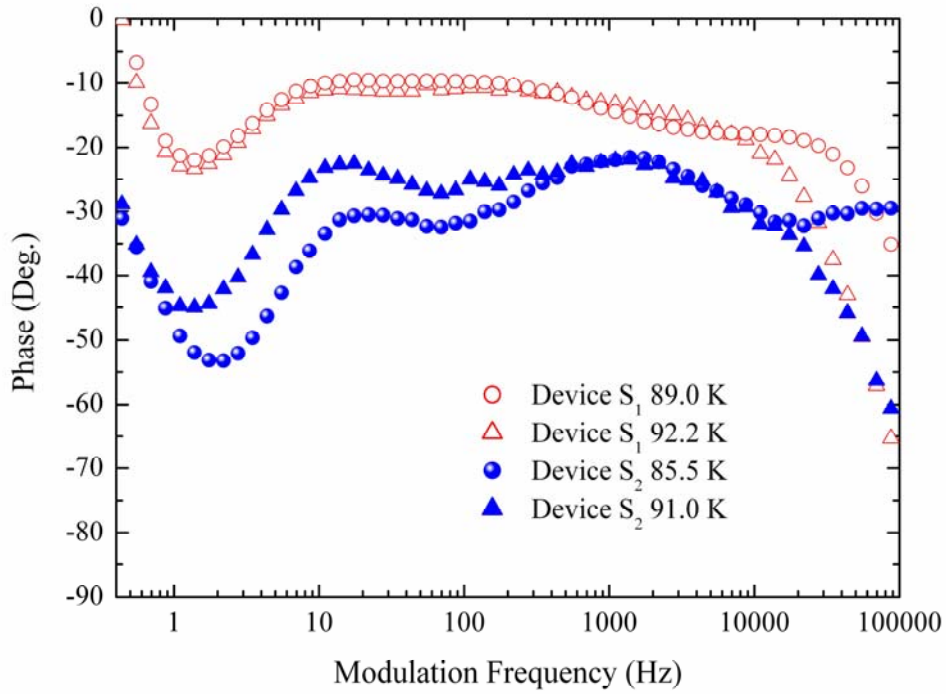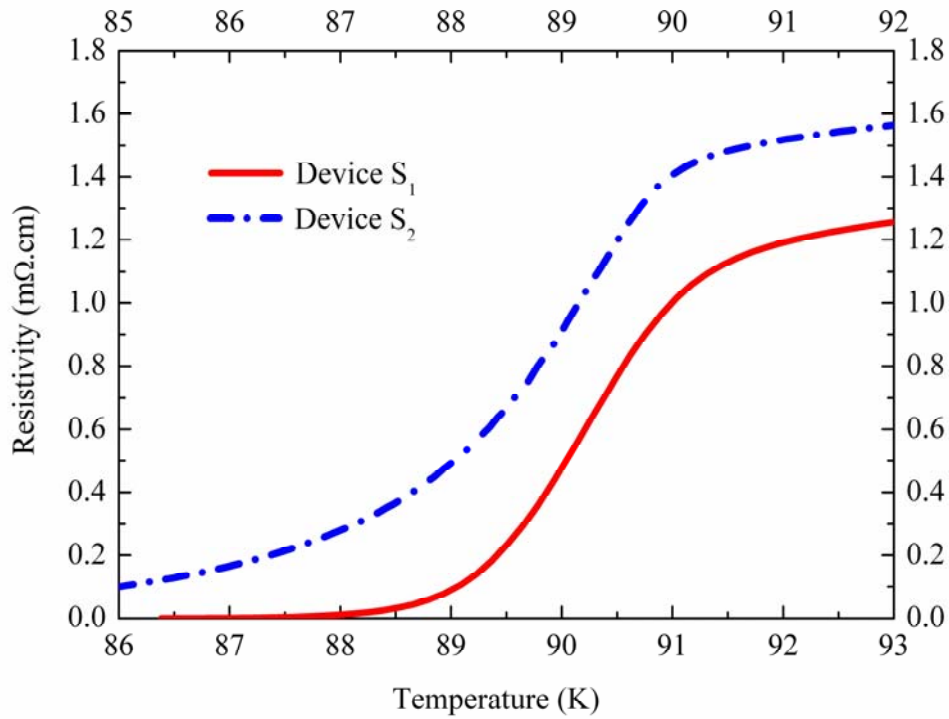

Figure 4.16: Resistivity versus temperature curves of the bolometers S_1 and S_2. Upper and bottom scales represent the temperature of the devices S_2 and S_1 respectively.

There have been a number of reports on possible correlation between ab-plane electrical and thermal resistivities using the Wiedemann –Franz law (Takenake et al. 1997, Zhang et al. 2000). Thus, we interpret that the reasons causing broad superconducting transition increase the resistivity of the YBCO thin film that in turn changes the thermal parameters and thermal resistivity of the film. Then these variations in the thermal parameters might be the causes for the phase dip around 1 Hz, which changes the magnitude and phase of the response of the bolometers. While the obtained results appeared to be highly dependent on the width of the superconducting transition of the films, it was found to be independent of the device patterns.

4.5 Wavelength Dependence of the Photoresponse of YBCO Edge Transition Bolometers

Figure 4.17: Photoresponse of the bolometers L_1 (at 88.5 K) and L_2 (at 87.2 K) as a function of wavelength at $I_b = 1$ mA and $f_m = 11$ Hz.

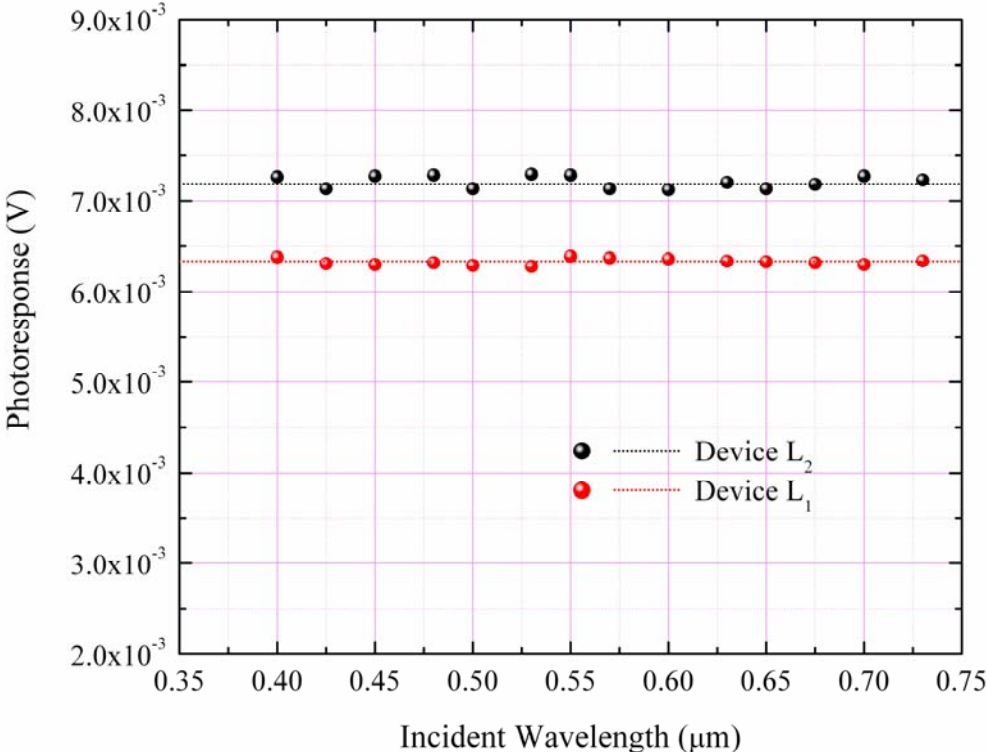The photoresponses of bolometers L_1 and L_2 for different wavelengths are plotted in Figure 4.17. It is noticed that the response of the devices is almost independent of the wavelength, from 0.4 to 0.73 μm, of incident light at bias current of 1 mA and modulation frequency of 11 Hz. The operating temperatures for devices L_1 and L_2 are 88.5 K and 87.2 K respectively. The obtained response results showed the similar behavior as reported in reference (Chen et al. 1997).

The interaction of incident photons and superconductor can be explained by using the concept of energy band gap and relation to cooper pairs. According to BCS, cooper pair binding energy $2\Delta(0)$ is on the order of meV, while optical photons in visible range have energies in the order of few eV. Illumination of a superconductor with optical photons therefore results in Cooper pairs breaking, creating quasiparticles with high energies relative to the gap (Gilabert 1990). These quasiparticles quickly decay via electron-electron collisions (breaking more Cooper pairs) and electron-phonon collisions (the phonons may go on to break other Cooper pairs). As the decay interactions are of energies in the gap range, both decay paths cause further breaking of pairs. In a very short time, the absorbed optical photons will have created a large excess of quasiparticles and phonons of energies close to $2\Delta(0)$ (Kopnin 2001). Pairs of these quasiparticles with energies near the gap can then condense back into Cooper pairs through phonon emission. We interpret that optical response is associated with variation in the flux of incident photons which have higher energy than the cooper pair binding energy. Therefore, the variation of the incident energy does not significantly affect the optical response of bolometers. Independence of the photoresponse of the devices from the wavelength of incident light proves the bolometers to be a broad band detector. This inherent property enables bolometer to be used for a wide range of wavelengths in the visible light region without degradation of the response, hence gives it superiority compared to other thermal detectors.

REFERENCES

Aboudihab, I., Gilabert, A., Azema, A., and Roustan, J.C. 1994. "Superconducting YBa$_2$Cu$_3$O$_{7-x}$ thin film bolometer for infrared radiation", *Superconductor Science and Technology*, Vol. 7, Issue 2, pp. 80-83.

Akram, R., 2000. "HTSC superconducting edge-transtition infrared detectors; principles, fabrication, & charactarisation." Master's thesis, Bilkent University.

Anderson, P.W., 1997. "The Theory of Superconductivity in the High-T$_c$ Cuprates", Princeton University Press, New Jersey.

Bardeen, J., Cooper, L. N., and Schrieffer, J. R. 1957. "Theory of superconductivity", *Phys. Rev.*, Vol. 108, No.5, pp.1175.

Bednorz, J.G.,and Muller, K.A. 1986. "Possible High Tc Superconductivity in the Ba-La-Cu-O system", *Z. Phys. B.*, Vol. 64, pp. 189.

Brasunas, J. C., and Lakew, B. 1994. "High T$_c$ superconductor bolometer with record performance", *Applied Physics Letters*, Vol. 64, Issue 6, February 7, pp.777-778.

Bozbey, A. 2003. "YBCO Edge transition bolometers: effect of superconductivity transition on the phase and magnitude of the response", Master's thesis, Bilkent University.

Bozbey, A., Fardmanesh, M., Askerzade, I. N., Banzet, M., and Schubert, J. 2004. "Effects of the superconductivity transition on the response of YBCO edge transition bolometers", *Superconductor Science and Technology*, Vol. 16, Issue 12, pp. 1554-1558.

Chen, H. Z., Chou, H., Chow, T. C., Hong, M. T., Lin, K. S., Cheng, Y. F., Chen, Y. C., and Lin, T. L. 1997. "The broad band optical detection of precipitational free YBCO thin films", *Physica C: Superconductivity*, Vol. 274, Issue 1-2, p. 24-32

Chou, H., Chen, H. Z., Hong, M. T., Chen, Y. C., and Chow, T. C. 1996. "Surface morphology effect on the photoresponse of high temperature superconducting microbridges", *Applied Physics Letters*, Vol. 69, Issue 9, pp.1306-1308.

Chu, C. W., Bechtold, J., Gao, L., Hor, P. H., and Huang, Z. J. 1988. "Superconductivity up to 114 K in the Bi-Al-Ca-Sr-Cu-O compound system without rare-earth elements", *Physical Review Letters*, Vol. 60, p. 941-943.

Chua L.O., Desoer C.A., and Kuh E.S. 1987. "Linear and nonlinear circuits ", McGraw-Hill book Co., p.756.

Cogollo, R.P., Mariño, A.C., and Sánchez, H.M. 2003 "Transport properties of YBCO superconducting films at different oxygen concentration", *IEEE Trans. on Appl. Supercond*, Vol.13, pp. 2789-2791

Dai, P., Chakoumakos, B. C., Sun, G. F., Wong, K. W., Lu, D. F., and Xin, Y. 1995. "Synthesis and neutron powder diffraction study of the superconductor $HgBa_2Ca_2Cu_3O_{8+x}$ by Tl substitution", *Physica C: Superconductivity*, Vol. 243, p. 201-206.

Dwir, B., and Pavuna, D. 1992. "A sensitive YBaCuO thin film bolometer with ultrawide wavelength response", *Journal of Applied Physics*, Vol. 72, No. 9, p. 3855-3861.

Fardmanesh, M., Rothwarf, A., and Scoles, K. J. 1995a. "$YBa_2Cu_3O_{7-x}$ infrared bolometers: Temperature-dependent responsivity and deviations from the dR/dT curve", *Journal of Applied Physics*, Vol. 77, Issue 9, pp.4568-4575.

Fardmanesh, M., Rothwarf, A., and Scoles, K. J. 1995b. "Low and midrange modulation frequency response for YBCO infrared detectors: Interface effects on the amplitude and phase", *IEEE Transactions on Applied Superconductivity*, Vol. 5, No. 1, p. 7-13.

Fardmanesh, M., Scoles, K. J., Rothwarf, A. 1999. "Control of the responsivity and the detectivity of superconductive edge-transition $YBa_2Cu_3O_{7-x}$ bolometers through substrate properties", *Applied Optics*, Vol. 38, Issue 22, pp.4735-4742

Fardmanesh, M. 2001. "Analytic Thermal Modeling for dc-to-Midrange Modulation Frequency Responses of Thin-Film High- T_c Superconductive Edge-Transition Bolometers", *Applied Optics*, Vol. 40, Issue 7, pp.1080-1088.

Fenner, D. B., Li, Qi, Hamblen, W. D., Johansson, M. E., Hamblen, D. G., Lynds, L., and Budnick, J. I. 1993. "Optical and thermal performance advantages for silicon substrates in YBCO bolometer devices", *IEEE Transactions on Applied Superconductivity*, Vol. 3, No. 1, pt. 4, p. 2104-2106.

Gilabert, A. 1990. "Interaction between light and superconductors", *Annales De Physique*, Vol.15, pp. 255-283.

Han, Z., Selinder, T. I., Helmersson, U. 1994 "Formation of Cu-rich particles on the surface of $YBa_2Cu_3O_{7-x}$ thin film grown by in situ off-axis sputtering", *Journal of Applied Physics*, Vol. 75, Issue 4, February 15, pp.2020-2025.

Hazen, R. M., Finger, L. W., Angel, R. J., Prewitt, C. T., and Ross, N. L. 1988. "100-K superconducting phases in the Tl-Ca-Ba-Cu-O system", *Physical Review Letters*, Vol. 60, p. 1657-1660.

Huhtinen, H., Paturi, P., Lähderanta, E., and Laiho, R. 1999. "Laser deposition of thin superconducting films from a nanocrystalline YBaCuO target", *Supercond. Sci. Technol.*, No:2, p. 81.

Hu, Q., and Richards, P. L. 1989. "Design analysis of a high Tc superconducting microbolometer", *Applied Physics Letters*, Vol. 55, Dec. 4, pp. 2444-2446.

Ivanov, K.V., Lima, A. M. N., Neff, H.,Deep, G. S., Khrebtov, I. A., and Tkachenko, A. D. 2002. "Effects of electrothermal feedback on operation of high-T_c superconducting transition edge bolometers", *Physica C*, Vol. 372, p. 432-435.

Josephson, B. D. 1962. "Possible new effects in superconductive tunneling", *Phys. Lett.*, Vol. 1, pp. 251-253.

Kiyokata, W. and Hayakawa, S. 1992. "Handbook of sputter deposition technology: principles, technology, and applications", *Noyes Publications*, New Jersey, USA.

Kopnin, N.B. 2001. "Theory of Nonequilibrium Superconductivity", *Oxford University Press*, USA

Kraus, H. 1996. "Superconductive bolometers and calorimeters", *Superconductor Science and Technology*, Vol. 9, Issue 10, pp. 827-842 (1996).

Kreisler, A. J., and Gaugue, A. 2000. "Recent progress in high-temperature superconductor bolometric detectors: from the mid-infrared to the far-infrared (THz) range", *Superconductor Science and Technology*, Vol. 13, Issue 8, pp. 1235-1245.

Kresin, V.Z., and Wolf S.T. 1990. "Fundamentals of superconductivity", Plenum Publishing, New York, USA.

Liu, X.Z., Li, Y.R., Tao, B.W., Luo, A., and He, S.M. 2002. "The effect of deposition rate on the microstructure of YBCO thin films prepared by inverted cylindrical magnetron sputtering" Physica C, Vol. 371, pp. 133-138.

Lu, P., Li, Y. Q., Zhao, J., Chern, C. S., Gallois, B., Norris, P., Kear, B., and Cosandey, F. 1992. "High density, ultrafine precipitates in YBa2Cu3O(7-x) thin films prepared by plasma-enhanced metalorganic chemical vapor deposition", *Applied Physics Letters*, Vol. 60, March 9, 1992, p. 1265-1267.

Mattox, D.M. 1998. "Handbook of Physical Vapor Deposition (PVD) Processing", *Noyes Publications*, New Jersey, USA.

Mischke, M., 2003. "Wavelength dependence of the photoresponse of a Yttrium - Barium-Copper-Oxide thin film", Master's Thesis, Notre Dame University.

Nahum, M., and Richards, P. L. 1991a. "Thermal boundary resistance of $YBa_2Cu_3O_{7-\delta}$ films", *Appl. Phys. Lett*, Vol. 59, No. 16, pp. 2034-2036.

Nahum, M., Hu Q., Richards, P.L., Sachtjen S.A., Newman N., and Cole B.F. 1991b. "Fabrication and measurement of high Tc superconducting bolometers", *IEEE Trans. Magn.*, Vol. 27, pp. 3081–3084.

Nahum, M., Verghese, S., Richards, P. L., and Char, K. 1991c. "Thermal boundary resistance for $YBa_2Cu_3O_{7-x}$ films", *Applied Physics Letters*, Vol. 59, Issue 16, pp. 2034-2036.

Onnes, H. K., 1911. "The dissapearance of the resistivity of mercury," *Comm. Leiden*, Vol. 122b.

Phelan P.E. 1995. "Thermal response of thin-film high-Tc superconductors to modulated irradiation", *J. Therm. Phys. Heat Transfer,* Vol. 9, pp. 397-402.

Richards, P. L., Clarke, J., Leoni, R., Lerch, Ph., Verghese, S., Beasley, M. R., Geballe, T. H., Hammond, R. H., Rosenthal, P., and Spielman, S. R. 1989. "Feasibility of the high T_c superconducting bolometer", *Applied Physics Letters*, Vol. 54, Issue 3, pp.283-285.

Richards, P. L., 1994. "Bolometers for infrared and millimeter waves", *Journal of Applied Physics*, Vol. 76, Issue 1, July 1, 1994, pp.1-24.

Robbes, D., Cheenne, N., Hamet, J.F., and Rice, J.P. 1999. "Thermal boundary resistance of a $YBa_2Cu_3O_{7-\delta}$/$SrTiO_3$ multilayer strip", *IEEE Transactions on Applied Superconductivity*, Vol. 9, Issue 2, Part 3, pp. 3874 - 3877

Rossnagel, S.M., Cuomo, J.J., and Westwood, W.D., Ed.1990. "Handbook of Plasma Processing Technology - Fundamentals, Etching, Deposition, and Surface Interactions", *Noyes Publications*, New Jersey, USA.

Schuegraf, K.K., Ed. 1988. "Handbook of thin-film deposition process and applications", *Noyes Publications*, New Jersey, USA .

Seshan, K., Ed. 2002. "Handbook of Thin-Film Deposition Processes and Techniques - Principles, Methods, Equipment and Applications", *Noyes Publications*, New Jersey, USA.

Suleiman, B. M., UI-Haq, I., Karawacki, E., Maqsood, A., and Gustafsson, S. E. 1993 "Thermal conductivity and electrical resistivity of the Y- and Er-substituted 123

superconducting compounds in the vicinity of the transition temperature", *Phys Rev B*, Vol. 48, No. 6, pp. 4095-4102.

Selinder, T. I.,Helmersson, U., Han, Z., Sundgren, J.E., Sjöström, H., and Wallenberg, L. R. 1992. "Yttrium oxide inclusions in $YBa_2Cu_3O_x$ thin films Enhanced flux pinning and relation to copper oxide surface particles", *Physica C*, Vol. 202, Issue 1-2, p. 69-74.

Takenaka, K, Fukuzumi, Y., Mizuhashi, K., Uchida, S., Asaoka, H., and Takei, H. 1997. "In-plane thermal conductivity and Lorenz number in $YBa_2Cu_3O_{7-y}$", Phys. Rev. B, Vol. 56, pp. 5654-5661

Tuohiniemi, M. 1999. "Laser-Ablation System for Depositing High-Temperature Superconducting YBaCuO Thin Films", Master's Thesis, Helsinki University of Technology.

Tsukamoto, A., Tsurukiri, E., Soutome, Y., Saitoh, K., Kurosawa, I., Takagi, K.   2003 "Composition and phase variations in Y-Ba-Cu-O thin films grown by off-axis sputtering as a function of deposition parameters", *Physica C*, 392–396, pp.1245–1249.

Uchiyama, T. and Iguchi, I. 2004. "Control of crystal orientation in YBCO thin films by an oxygen diffusion process", *Supercond. Sci. Technol.*, Vol. 17, pp. 592-595

Uher, C., and Kaiser, A. B. 1987. "Thermal transport properties of $YBa_2Cu_3O_7$ superconductors" *Phys. Rev. B*, Vol. 36, No. 10, pp. 5680-5683.

Ye, J., and Nakamura, K. 1993. "Quantitative structure analyses of $YBa_2Cu_3O_{7-delta}$ thin films: Determination of oxygen content from x-ray-diffraction patterns", *Phys. Rev. B*, Vol. 48, pp. 7554-7564

Wu, M. K., Ashburn, J. R., Torng, C. J., Hor, P. H, and Meng, R. L. 1987. "Superconductivity at 93 K in a new mixed-phase Y-Ba-Cu-O compound system at ambient pressure", *Physical Review Letters*, Vol. 58, p. 908-910.

Zhang, Y., Ong, N. P., Xu, Z. A., Krishana, K., Gagnon, R., and Taillefer, L. 2000. "Determining the Wiedemann-Franz Ratio from the Thermal Hall Conductivity: Application to Cu and $YBa_2Cu_3O_{6.95}$", *Phys. Rev. Lett.*, Vol. 84, pp. 2219-2222